ATOMIC LAYER DEPOSITION BASED TITANIUM ALLOYING OF ZNO FOR MICROBOLOMETER APPLICATIONS

A THESIS SUBMITTED TO

THE GRADUATE SCHOOL OF ENGINEERING AND SCIENCE

OF BILKENT UNIVERSITY

IN PARTIAL FULFILLMENT OF THE REQUIREMENTS FOR

THE DEGREE OF

MASTER OF SCIENCE

IN

MATERIALS SCIENCE AND NANOTECHNOLOGY

By
Bilge Temiz
July 2016

ATOMIC LAYER DEPOSITION BASED TITANIUM ALLOYING
OF ZnO FOR MICROBOLOMETER APPLICATIONS
By Bilge Temiz
July 2016

We certify that we have read this thesis and that in our opinion it is fully adequate,
in scope and in quality, as a thesis for the degree of Master of Science.

Ali Kemal Okyay (Advisor)

Kağan Topallı

Yunus Eren Kalay

Approved for the Graduate School of Engineering and Science:

Levent Onural
Director of the Graduate School

ABSTRACT

ATOMIC LAYER DEPOSITION BASED TITANIUM ALLOYING OF ZNO FOR MICROBOLOMETER APPLICATIONS

Bilge Temiz
M.S. in Materials Science and Nanotechnology
Advisor: Ali Kemal Okyay
July 2016

Microbolometers are attractive candidates for both military applications and consumer electronics among the uncooled thermal detectors due to their compactness, low cost, comparable performance with photon detectors and CMOS compatibility. The temperature sensitive active material is the most important part of resistive type microbolometers where change in electrical response occurs upon IR radiation. Typical active materials used for this purpose are YBCO and VO_x. It was reported in several studies that ZnO has higher TCR value than commercially available active materials. However a temperature insensitive TCR property has not been achieved yet.

To improve the TCR property of ZnO, doping with Titanium is proposed in this work. According to Ellingham diagram of oxides which is used generally in extractive metallurgy, it is obvious that titanium oxide is more stable than zinc oxide [1]. Therefore doping with Titanium may reduce oxygen related defects and improve TCR property. Atomic layer deposition (ALD) is used for digital alloying of ZnO with Titanium. Titanium doped ZnO (TZO) films with Ti concentrations 2.5%, 5.9% and 12.2% were deposited using precursors diethylzinc, mili-Q water and tetrekis(dimethylamido)titanium. Then intrinsic defect related elemental characterization were made. Effect of Titanium doping on structure of TZO thin films was discussed.

After material characterization, planar microresistors were fabricated in UNAM cleanroom facility. Piranha-HF and solvent cleaning of silicon substrate were performed before microfabrication. Vaksis Handy Plasma Enhanced Chemical Vapor Deposition (PECVD) was used to deposit insulation layer on silicon

wafer. Photolithograpy steps were performed using Laurell Spinner system and EVG 620 mask aligner to pattern TZO thin film. Then contact material metallization was performed using Vaksis MIDAS Thermal Evaporator system.

Current-voltage characterization of microfabricated resistors was performed before Temperature Coefficient of Resistance (TCR) measurements to see the contact type resistors. Then TCR measurements were done between 15^oC and 25^oC by applying constant current to the contact pads of resistor. Approximate resistivity values of 5 different samples were calculated. It is shown that proposed TZO active material for resistive type microbolometers has a temperature insensitive and high TCR value.

ÖZET

MİKROBOLOMETRE UYGULAMALARI İÇİN ÇİNKO OKSİDİN ATOMİK KATMANLAMA YÖNTEMİYLE TİTANYUM İLE ALAŞIMLANMASI

Bilge Temiz

Malzeme Bilimi ve Nanoteknoloji, Yüksek Lisans

Tez Danışmanı: Ali Kemal Okyay

Temmuz 2016

Mikrobolometreler düşük maliyetliliği, CMOS prosesine uygunluğu, foton detektörleriyle karşılaştırılabilir performansından dolayı, hem ticari hem de tüketici elektroniği uygulamaları için soğutmasız kızılötesi detektörler arasında en iyi adaydır. Direnç tipi mikrobolometrelerin en önemli bölümü sıcaklığa duyarlı aktif malzemedir. Bu sıcaklığa duyarlı bölüm sayesinde elektrik sinyalindeki değişim okuma devresi tarafından okunur ve termal görüntü oluşturulur. Literatürdeki birçok çalışmada çinko oksidin sıcaklığa bağlı direnç değişim katsayısının oldukça yüksek olduğu rapor edilmiştir. Fakat hala sıcaklıkla değişmeyen TCR özelliği elde edilememiştir.

Bu çalışmada çinko oksidin TCR özelliğinin geliştirilmesi için titanyumla katkılama önerilmiştir. Çünkü titanyumdioksit metal oksitlerin Ellingham diyagramına göre her sıcaklıkta çinko oksitten termodinamik olarak daha kararlıdır. Titanyum, çinko oksit yapısı içerisinde oksijene bağlı kusurların azaltılmasını ve dolayısıyla çinko oksidin TCR özelliğinin geliştirilmesini sağlayabilir. Titanyum katkılı çinko oksit ince filmler atomik katman biriktirme yöntemiyle büyütülmüştür. %2.5, %5.9 ve %12.2 titanyum içeren çinko oksit ince filmler elde edilmiştir. Büyütülen ince filmlerin malzeme karakterizasyonu yapılmıştır.

Büyütülen filmlerden mikro direnç yapıları üretmek için ilk önce silikon alttaş Piranha-HF ve solvent temizliğine tabi tutulmuştur. Daha sonra alttaş ile direnç yapısı arasındaki elektriksel izolasyonu sağlamak için plazma yardımcılı kimyasal buhar biriktirme yoluyla silikon oksit katmanı kaplanmıştır. Daha sonra atomik katman biriktirme yöntemiyle titanyum katkılı çinko oksit büyütülmüştür. Bu

katman fotolitografi yoluyla şekillendirilmiş ve kontak metali termal buhar biriktirme yoluyla kaplanmıştır.

Üretilen mikro dirençlerin ilk önce akım-voltaj karakterizasyonu daha sonra sıcaklığa bağlı direnç katsayısı ölçümü yapılmıştır. Malzemenin özdirenci yaklaşık olarak hesaplanmıştır. Üretilen yapılar sıcaklıkla değişmeyen ve yüksek sıcaklığa bağlı direnç katsayısına sahiptir.

Anahtar sözcükler: Direnç tipi soğutmasız kızılötesi detektörler, mikrobolometreler, aktif malzeme karakterizasyonu.

Acknowledgement

I wish to thank my advisor Dr. Ali Kemal Okyay for his valuable guidance throughout development of my thesis. I have gained both theoretical and practical invaluable information from him. I would like to thank especially my committee members Kağan Topallı and Yunus Eren Kalay for their helpful comments.

I would like to specially thank to my mentors Sami Bolat and Feyza Oruç for their guidance, persistent help. I have learned a lot from them.

I would also like to thank Okyay Group members Amir Ghobadi, Şeyma Canik Arslan, Ali Cahit Köşger, Abdullah Gök, Gamze Türkan Ulusoy, Sina Abedini Dereshgi, Hamid Reza Rasouli, Zülkarneyn Şişman , Kazım Görgülü, and previous group members Ayşe Özcan, Fatih Bilge Atar, Burak Tekcan, Elif Özgöztaşı, Özge Abanoz, Amin Nazirzadeh, Berk Berkan Turgut for being nice friends to me.

I would like to thank my close friends Latif Önen, Murat Serhatlıoğlu, Hamit Eren, Said Emre Alper, Ali Haider for nice conversations during coffee breaks.

I would like to thank my colleagues Fırat Tankut, Hande Öztürk , Hıdır Aşkar, Görkem Cilbir, Nihan Çakır, Hilal Kübra Dumanlı, Beril Uğur, Orkun Tomruk, Alper Küçükkömürler, Tugay Arslan, Haluk Çöloğlu for their friendship.

I would also like to thank our collaborators METU-MEMS, Mikrosens, Dr. Tayfun Akın, TopallıGroup members, BıyıklıGroup members Dr. Necmi Bıyıklı, Seda Kızır and Halil Volkan Hünerli for their invaluable helps in my research.
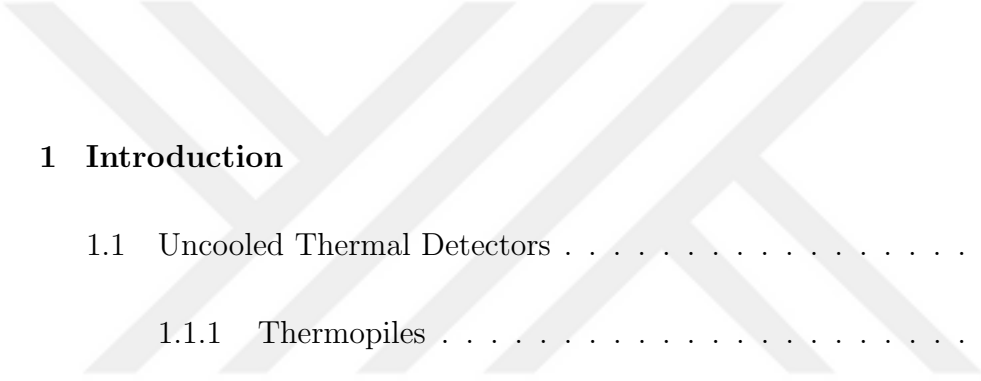
I would also like to thank UNAM Cleanroom Team members, Semih Yaşar, Fikret Piri and Abdullah Kafadenk.

I would like to thank my beloved family members Ayşe Temiz, Turhan Temiz, Ozan Temiz, Zehra Afacan and Peri for their encouragement and moral support.

Very special thanks to my better half Tuna for his great patience and endless support during this work.

Contents

List of Figures

List of Tables

Chapter 1

Introduction

Infrared radiation is a portion of electromagnetic spectrum which lies between the red end of visible spectrum and terahertz radiation, therefore its wavelength ranges from 1 to 20 μm. It allows us to obtain night vision because all objects having temperature higher than absolute zero (0^oKelvin) radiate infrared energy [2]. Infrared spectrum consists of four parts namely short-wave infrared (1-3 μm), mid-wave infrared (3-5 μm), long-wave infrared (8-14 μm) and finally far infrared (16-20 μm) [3]. For thermal vision applications long-wave infrared detectors are preferred because objects at room temperature radiate infrared energy with wavelength around 10 μm [4].

Infrared detectors are classified as photon detectors and thermal detectors. In photon detectors, semiconductors having low band gap are used, thus absorbed infrared radiation causes excitation and free electron-hole pair generation. The intensity of infrared radiation is directly determined and processed by the help of electronic circuit. Since photon infrared detectors use direct way of sensing infrared radiation, they are faster and more sensitive than thermal detectors. However, there is another electron-hole pair generation mechanism called thermal excitation which inhibits the use of photon detectors, because thermally generated electron-hole pairs are much higher than electron-hole pairs generated by infrared radiation at room temperature [5]. An extensive cooling unit makes

possible infrared imaging with photon detectors, but this increases cost, size and system operating power. This is why photon detectors are preferred for defence and space applications [6]. On the other hand, thermal detectors use an indirect way of infrared radiation sensing. The incoming radiation cause change in electrical parameter of active material, then this change processed by a electronic circuit. Thermal detectors are also known as uncooled infrared detectors with lower size, cost and comparable performance with photon detectors and this make them the best candidate for both military applications and consumer electronics. Although there are many commercially available thermal detectors in the market, their prices are still very high for consumer electronics. The aim of this thesis is to investigate a new active material for ultra low cost and mid-performance microbolometer type thermal detectors.

1.1 Uncooled Thermal Detectors

Heating effect of infrared radiation causes change in electrical properties of temperature sensitive material in detectors followed by infrared imaging. Depending on electrical response of material, uncooled thermal detectors are classified as thermopiles, pyroelectric detectors and microbolometers which were explained in section 1.1.1, 1.1.2 and 1.1.3 sequentially.

1.1.1 Thermopiles

Thermopiles composed from serially connected thermocouples. Figure 1.1 shows the representative thermopile drawing. Thermocouples are formed by the junction of two metals with different Seebeck coefficients, therefore, response of thermopiles to temperature change is voltage difference [7]. The suspended side of thermopile is heated due to absorbtion of infrared radiation and the substrate side remains nearly at the same temperature. Voltage difference is formed as a result of heating from one end because of different Seebeck coefficients of materials, as seen from the Figure 1.1 [8]. This phenomena is also known as thermoelectric
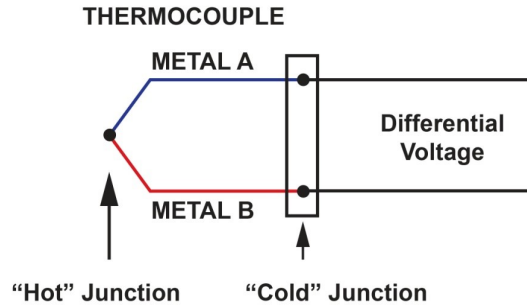
Figure 1.1: Schematic thermocouple illustration [8]

effect. Generated voltage difference is permanent as long as the hot and the cold sides are kept at the same temperature. The voltage difference is proportional to both temperature difference and Seebeck coefficient difference between the materials of junction as seen from equation 1.1 [9].

$$V_e nd = (\alpha_1 - \alpha_2)(T_h - T_c) \qquad (1.1)$$

For better performance, hot and cold sides of thermocouple should be thermally isolated from each other. This is possible by using materials having low thermal conductance with low thermal noise, but these properties are competing with each other. Thermal or Johnson noise are proportional to resistance and resistivity of the material. In order to reduce the noise, the ideal material should have a low resistivity. However, for higher Seebeck coefficient, the material should have high resistivity. To fulfill all requirements an optimum material should be selected.

Since thermopile system itself generate very stable voltage difference, it is not required to apply voltage bias to operate the system. However amount of voltage difference generated by one thermocouple is not enough for infrared detection, therefore a series of thermocouples are used in thermopiles. Also due to their low responsivity and relatively large size, thermopiles are not preferred as thermal detectors.

1.1.2   Pyroelectric Detectors

In pyroelectric materials, when a temperature change occurs, atoms in crystal structure move slightly from their original positions resulting in polarization change and voltage generation. However pyroelectric materials are different from thermoelectric ones, because for pyroelectricity, voltage generation occurs due to polarization change, not due to temperature difference between two ends. Also the voltage generation continues to occur as temperature of the crystal changes, which means if the whole crystal stays at the same temperature, there will be no voltage generation. Working principle of pyroelectric materials is shown in Figure 1.2 [10].

The polarization change in the pyroelectric materials originate from the net dipole moment in crystal structure. All ferroelectric materials are pyroelectric materials at the same time. As known, ferroelectric materials also have net dipole moment in crystal structure which causes ferroelectric materials have permanent magnetic properties. This net dipole moment in crystal structure is the result of anisotropic crystal structure. For anisotropy, there should be no rotational symmetry axis and center of symmetry axis. From 32 crystal point-group symmetry, just 10 of them have this property. Common materials showing pyroelectricity are tourmaline, lead zirconate titanate (PZT), lithium tantalate, gallium nitride, caesium nitrate, polyvinyl fluorides, collagens [11].

The net dipole moment in crystal structure exists below the Curie temperature of the material, hence pyroelectric infrared detectors works below this temperature [12]. For this purpose pyroelectric detectors include temperature stabilizers [13].

1.1.3   Microbolometers

Microbolometers are sensors that convert the infrared radiation into electric signal by measuring the amount of incoming radiation to detector. Support arms,
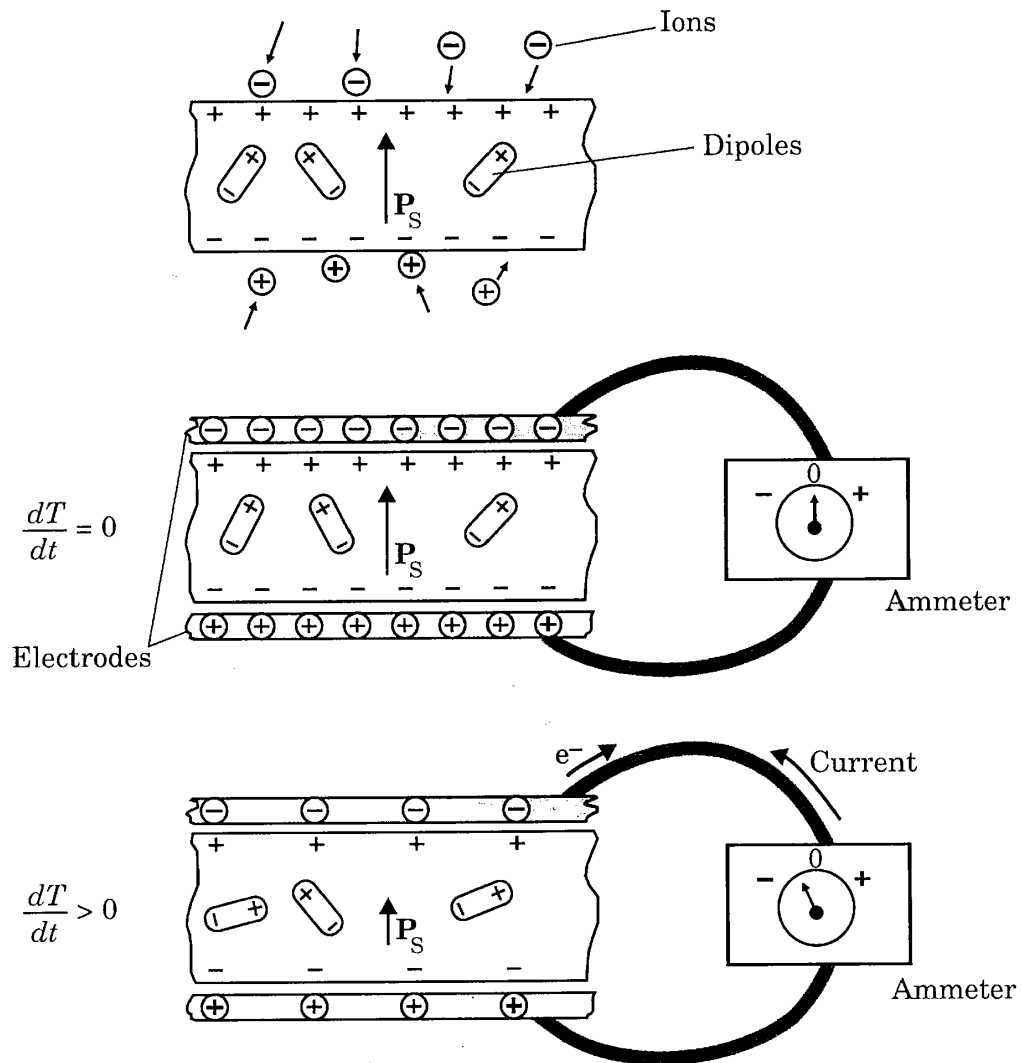
Figure 1.2: Schematic representation of pyroelectric detectors working principle [10]

infrared absorber, temperature sensitive active material are components of microbolometers. Infrared radiation reaches to the detector pixel and absorbed by the suspended structure. This causes infrared heating and temperature rise in active material. Temperature change affects the properties of active material and this signal is sensed by the read-out circuit on pixel. Support arms both isolate the suspended structure for better heating and provide electrical connection between the read-our circuit and body. Figure 1.3 shows the schematic drawing of microbolometers [14]. Active material of microbolometers can be both resistive type or diode type. For resistive type, the resistance of material changes, for diode type, the forward voltage changes as a result of infrared heating.

For resistive type of microbolometers there are a few commercial active material options such as vanadium oxide (VO_x), Yttrium Barium Copper oxide (YBCO), amorphous silicon (a-Si), poly Silicon-Germanium (Poly Si-Ge), metals.

Vanadium oxide is one of the most popular active materials that is used in microbolometers due to its high temperature coefficient of resistance (TCR)with -2-3%/K. However, Vanadium oxide is not compatible with CMOS technology, thus a separate line is necessary for Vanadium oxide deposition and microfabrication to prevent CMOS contamination [15]. Also Vanadium oxide has large 1/f noise due to its amorphous structure which is another drawback. As reported, it is possible to decrease sheet resistance of VO_x and improve TCR by using Vanadium-Tungsten Oxide. Raytheon, BAE, Indigo Systems, Mitsubishi are among the companies preferring to use VO_x as active material.

Yttrium Barium Copper Oxide is another option for active material with high TCR value with -3.4%/K and low 1/f noise. Although room temperature deposition of YBCO is possible, it is not CMOS compatible too [16]. Infrared image taken from the Raytheon's resistive type microbolometer is illustrated in Figure 1.4 [17].

Amorphous silicon attracts attention due to its CMOS compatibility and uniformity. ULIC and Raytheon are companies developing amorphous-silicon based

6
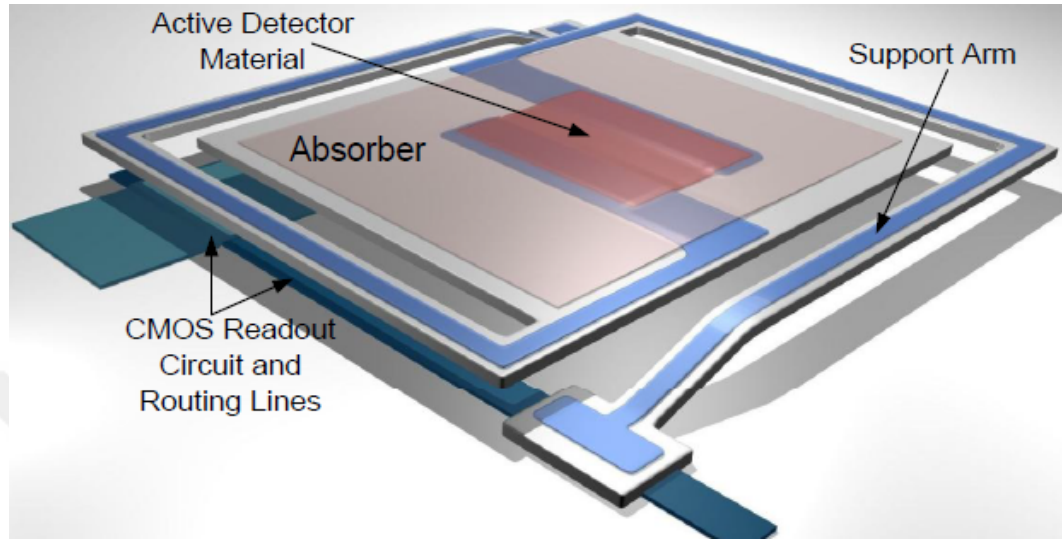
Figure 1.3: Representative drawing of microbolometers [14]

uncooled infrared detectors. The maximum reported TCR value of amorphous silicon is -3%/K [18]

Poly-Si-Ge with TCR value -2.5%/K is developed by IMEC, Belgium and transferred to XenIcs, Belgium. Due to its high deposition temperature, CMOS integration is somewhat challenging. Also internal stress is developed in poly SiGe film causing buckling effects. For stress relief, post-CMOS processing is necessary which adds steps to process flow and increases cost. The 1/f noise of poly-SiGe is high due to its non-crystalline structure.

Finally metals are used as active materials in resistive type microbolometers. They are preferred due to CMOS compatibility although they have low TCR values. For example TCR value of titanium and platinum is reported as 0.3%/K [19].

1.2   Low-Cost Uncooled Thermal Imaging

In this section low-cost uncooled thermal image technology developed in METU-MEMS Center and continued in spin-off company MikroSens is presented [20, 21].

Figure 1.4: Image from Raytheon's resistive type bolometer [17]

Low cost uncooled detector fabrication includes post-CMOS microfabrication steps. Process flow starts with Reactive Ion Etching (RIE) of CMOS wafer oxide layer. In this process CMOS metal routing layers are used as hard mask. After RIE, metal layers are removed. Finally for detector suspension, Silicon handle wafer is etched using anisotropic wet etch technique. Simplified post-CMOS process flow was illustrated in the Figure 1.5 [22].

Since uncooled microbolometer detectors need vacuum environment for thermal isolation, CMOS wafers are wafer level vacuum packaged. For packaging, specially designed cap wafer which encapsulates thermal sensors on CMOS wafer is used. CMOS wafer and cap wafer hermetically bonded to each other in vacuum environment using an adhesive layer.

1.3   Performance Parameters

In this section parameters that affect the performance of the low-cost resistive type microbolometers are introduced. Temperature sensitivity (TC), one of the most important parameter of microbolometer active material, is mentioned in the section 1.3.1. Then resistivity and resistance are expressed in the section 1.3.2.
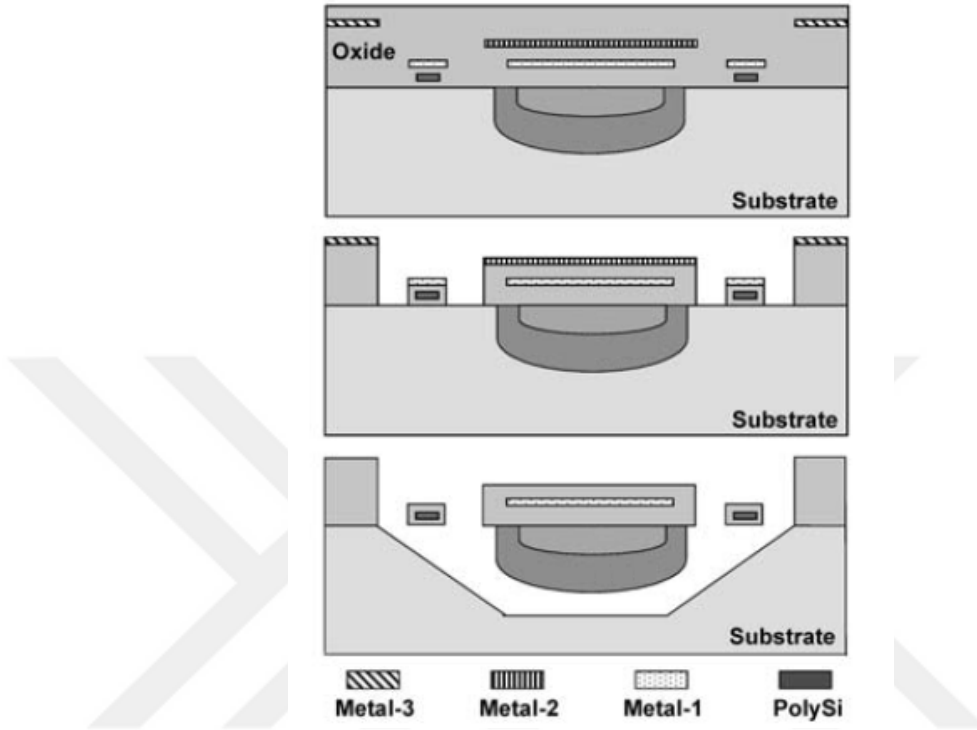
Figure 1.5: Simplified post-CMOS process flow [22]

1.3.1 Temperature Sensitivity

Temperature sensitivity means measurable electrical property change in active material for unit change in temperature due to infrared heating. For resistive type microbolometers, temperature sensitivity is defined as temperature coefficient of resistance as shown in the equation 1.2. Resistance increases or decreases with raising temperature resulting negative or positive TCR values depending on material type.

$$\alpha = \frac{1}{R}\frac{dR}{dT} \tag{1.2}$$

Where alpha is temperature coefficient of resistance in %/K, R is the resistance of the active material on detector, T is the temperature at which infrared detector operates.

9

For metals as temperature raises, resistivity increases due to lattice vibrations in crystal structure and causes metals having positive TCR values generally. On the other hand, semiconductors have negative TCR values because resistivity decreases when temperature raises.

In summary TCR property of material is strongly related with the resistivity, doping level and material type. It can be optimized by adjusting deposition parameters, doping.

1.3.2   Resistivity and Resistance

Resistivity is defined as obstacle to electron flow and it is an intrinsic property of material. On the other hand resistance is an extrinsic property depends on directly resistivity. The relation between resistance and resistivity was given in the equation.

$$R = \frac{\rho l}{A} \tag{1.3}$$

Where R is resistance, ρ is resistivity, l is length in electron flow direction, A is cross-section of current flow.

1.4   Motivation of Thesis Work

ZnO is a strong candidate for optoelectronic applications due to its wide gap with 3.37 eV and lasing applications which depends on exciton recombination [23]. The exciton binding energy of ZnO is higher than the commercial materials used in optical applications. Its wide band gap make ZnO trasparent, so it can also be used as transparent conductive oxide [24]. Undoped ZnO is a natural n-type semiconductor and the reason of n type conductivity still remains unclear. Some research groups reported that intrinsic defects such as oxygen vacancies (V_o) and zinc interstitials (Z_i) may be the reason of this residual n-type condictivity, where others claimed that unintentionally introduced hydrogen impurity in ZnO due to the growth conditions causes this behaviour [25].

Another application of ZnO is thin film transistors used in liquid crystal display technology [26]. ZnO TFTs are being replaced with commercial a-Si TFT's due to their high mobility, process compatibility with flexible substrates [27]. However for ZnO TFTs negative bias instability is reported due to charge trapping [28, 29].

ZnO is a candidate attractive active material for low-cost uncooled thermal detectors due to its high TCR value [30]. Also its CMOS compatibility due to low temperature deposition and tunable resistivity ranging from 0.01 to 100 Ω-cm for deposition temperatures ranging from 200^oC to 120^oC are important [31]. Several studies were conducted about high TCR features of ZnO. For pulsed laser deposited ZnO, TCR values ranging from -3.4%/K to 13%/K were reported [32]. For ALD deposited ZnO, a maximum TCR value -10.4%/K is obtained [33]. Another active material candidate for low-cost uncooled thermal detectors is TiO_2 with a maximum TCR value -9%/K as reported in a very recent manuscript [34]. Although TCR values of ZnO and TiO_2 are higher than that of the commercial active bolometer materials, a temperature insensitive TCR value at room temperature has been not achieved yet. To improve TCR property of ZnO, doping with Hf, In, Cr, Al, Ga is proposed [35]. Several studies were conducted to improve bias stability of ZnO thin film transistors with Hf doping. In these studies, reduction in oxygen related defects and charge trapping were reported due to

high binding energy of Hf ions to oxygen [36, 37]. Atomic layer deposition is a powerful technique for digital alloying of ZnO at various doping concentrations and low temperature deposition of ZnO thin films with high crystal quality, precise thickness control, uniformity and conformity [38].

So the aim of this work is;

1. to optimize an active material for resistive type microbolometers having a temperature insensitive and high TCR value by digitally alloying ALD grown ZnO with various concentrations of a selected element
2. to make intrinsic defect related elemental and structural characterization of grown material
3. to fabricate microresistors from grown materials and investigate the effects of doping on temperature coefficient of resistance.

1.5   Thesis Overview

This thesis reports the electrical and material characterization of atomic layer deposited Titanium doped ZnO (TZO) thin films as an active layer of uncooled resistive type microbolometers.

Chapter 2 presents description of equipment used for microfabrication of resistors and used for material characterization of ALD-grown TZO thin films. Also fabrication details were given for the fabrication of planar resistors.

Chapter 3 includes scientific background about stability of metal oxides and selection of doping element. Also intrinsic defect related elemental and structural characterization of ALD-grown TZO material.

Chapter 4 consists of electrical characterization of microfabricated resistors. I-V curve and TCR measurement results were given in this chapter including details of TCR measurement set-up.

Chapter 2

Experimental Methods

In this chapter, equipment used for microfabrication of resistors are introduced in section 2.1 where microfabrication steps are mentioned in section 2.2. Characterization methods are described in section 2.3.

2.1   Equipment Used

For resistor microfabricaton, Plasma Enhanced Chemical Vapor Deposition system (PECVD), Atomic Layer Deposition system (ALD), Thermal evaporator, Mask Aligner, photolithography and lift-off steps are introduced for patterning steps. For material characterization X-ray Photoelectron Spectroscopy (XPS) and Grazing Incidence X-ray Diffraction are described.

Figure 2.1: Vaksis Handy CVD/PECVD system [39]

2.1.1 Plasma Enhanced Chemical Vapor Deposition (PECVD)

To isolate bottom Silicon wafer and the resistor structure, the dielectric material SiO_2 was deposited by Vaksis Handy Plasma Enhanced Chemical Vapor Deposition System (PECVD).

Plasma enhanced chemical vapor deposition is a powerful technique for low temperature deposition of oxides and nitrides from their gaseous precursors. Plasma is created by application of RF or DC power and after plasma creation, gaseous reactants are ionized and deposition reaction occurs at lower temperatures. Thin films deposited by PECVD are more uniform and conformal, less rough then films deposited by sputtering systems. Also low temperature deposition make possible to coat metal or other temperature sensitive devices with dielectrics. Finally PECVD systems are good candidate for industrial applications due to their high deposition rate. The plasma enhanced chemical vapor deposition system in Bilkent University-UNAM (National Nanotechnology Research Center) clean room facility is shown in Figure 2.1. [39]

2.1.2 Atomic Layer Deposition (ALD)

The deposition of active material layer for resistive type microbolometers was performed by Cambridge Nanotech Savannah 100 Thermal Atomic Layer Deposition system.

Atomic layer deposition (ALD) is a type of chemical vapor deposition technique used for deposition of semiconductors, dielectric materials and some metals. In contrast to chemical vapor deposition, precursors react with the surface of the substrate and are introduced to the chamber sequentially. Generally two precursors are used in ALD systems. For example diethylzinc and water vapor are used in deposition of ZnO. Deposition mechanism of ALD system is illustrated schematically in Figure 2.2 [40].

As seen from Figure 2.2, the first gaseous reactant (water vapor for ZnO) enters the chamber in pulse step, reacts with the surface atoms, reaction continues until all surface atoms of the substrate are covered by the precursor atoms. This is why ALD is known as self-limiting deposition technique. Remnant precursor atoms are evacuated from the chamber in the purge step. Then the second precursor was introduced and purged from the chamber. At the end of two pulse and two purge steps, single atomic layer of material is deposited. According to desired thickness, these pulse/purge steps are repeated.

Since deposition is performed layer by layer, deposition rate of ALD systems is very slow (a few $\mathring{A}$/cycle). However, such a deposition rate allows the deposition of very thin and conformal layers with improved excellent uniformity. Even substrates with high aspect ratio are coated continuously using ALD system. The thermal ALD system is shown in the Figure 2.3 [41]. The precursors used for deposition of Titanium doped ZnO are listed in Table 2.1.
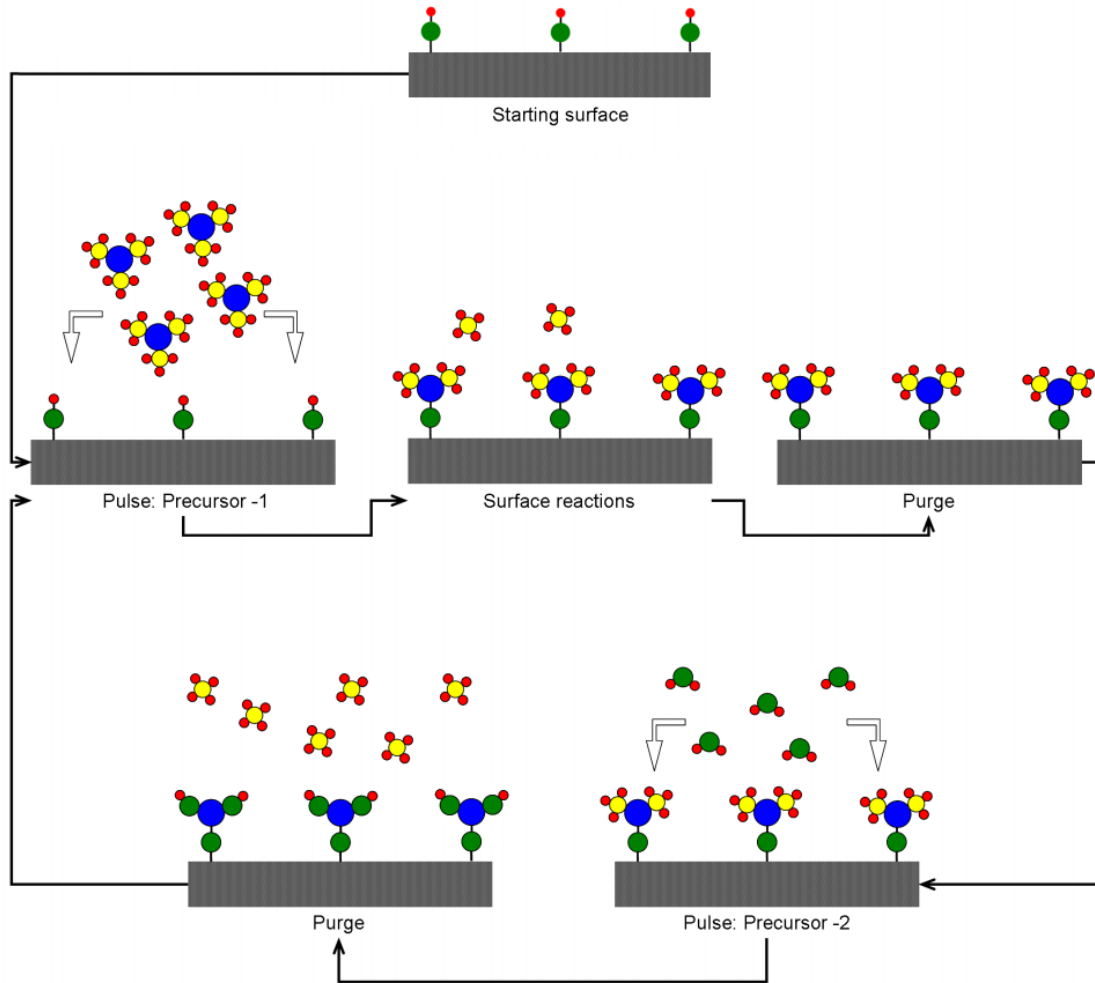
Figure 2.2: Representative ALD deposition mechanism [40]

Table 2.1: Precursors used for deposition of TZO

Element	Precursor
Zinc	Diethylzinc $(C_2H_5)_2Zn$
Titanium	Tetrakis(dimethylamido)titanium $(C_2H_6N)_4Ti$
Oxygen	mili-Q water H_2O

Figure 2.3: Cambridge Nanotech Savannah 100 ALD system [41]

Table 2.2: Deposition parameters of contact material

Material	Acoustic Impedance	Density (gr/cm^3)	Tooling factor
Aluminum	8.17	2.7	%100

2.1.3 Thermal Evaporation

Contact material deposition after lithography step was made using Vaksis MIDAS Thermal Evaporator PVD/3T system. Aluminum is used as contact material for Titanium doped ZnO.

Thermal evaporation is a type of physical vapor deposition technique used for deposition of metals having low melting point. Metal source generally in pellet form is put into conductive boat made from Tungsten or Molybdenum. Boat is heated to evaporate metal under vacuum conditions to avoid metal oxidation and introduction of impurities to film. Also vacuum operation increases the mean free path, therefore eases the directional travel of metal atoms to the substrate surface. Metal atoms condense back when they hit to the substrate surface. Rotation of substrate improves uniformity of thin film. Deposition rate is adjusted using the crystal thickness monitor. The thermal evaporator system used for metallization is illustrated in Figure 2.4 [42]. The deposition parameters used for Aluminum contact material are listed in Table 2.2 below.

Figure 2.4: Vaksis MIDAS Thermal Evaporator PVD/3T System [42]

2.1.4　Mask Aligner and Photolithography

After deposition of SiO_2 insulation layer by PECVD and active material by ALD, sample was patterned using photolithography followed by lift-off. For lift-off process of contact material, pre-deposition lithography was made.

Lithography is a microfabrication process used for transferring desired patterns to the substrate surface by coating a light-sensitive polymer photoresist on it, exposing the photoresist with UV source and chemically treating the photoresist in developer. After exposure of the photoresist, its solubility in developer changes. Schematic photolithography steps are illustrated in Figure 2.5 [43].

In lift off, first a sacrificial resist is deposited on the substrate following by removing the undesired part of resist, and depositing the target material on the whole surface. Finally substrate is put into solvent to wash away the resist and to lift off the excess material on it. All lithography steps were described sequentially.
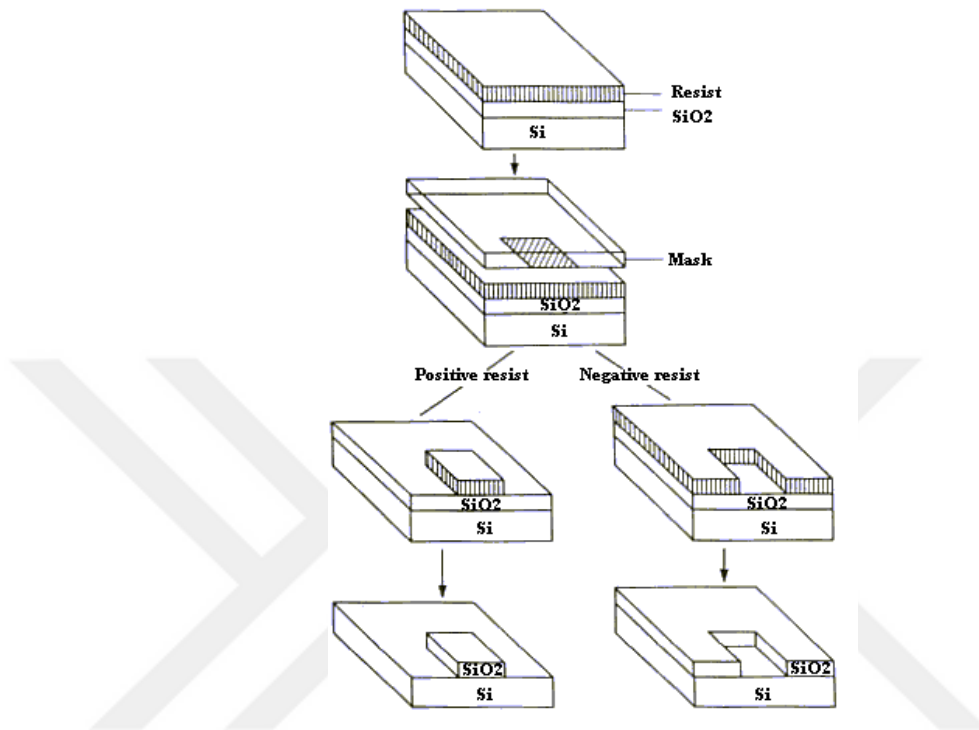
Figure 2.5: Representative photolithography steps [43]

2.1.4.1 Substrate Cleaning

Piranha cleaning was performed to remove organic remedies from the substrate. For piranha solution 1:1 mixture of Sulphuric acid (H_2SO_4) and hydrogen peroxide (H_2O_2) are used. Piranha cleaning was followed by HF cleaning to remove native oxide layer formed due to piranha cleaning. Finally samples were washed with DI water and dried with Nitrogen gas.

For solvent cleaning, samples were put into acetone and sonicated for 5 minutes. This step was repeated for solvents isopropanol alcohol and methanol. The last step was washing samples with DI water and drying them with Nitrogen gas.

Figure 2.6: Laurell Spinner System

2.1.4.2 De-hydration Step

De-hydration step is important part of lithography step, the substrate surface should be dry enough for better adhesion of photoresist. For de-hydration, sample was put into oven which is at 110^oC to evaporate water droplets from the surface. De-hydration temperature should be higher than the boiling temperature of the water for better evaporation of water from the substrate surface.

2.1.4.3 Photoresist Coating

Before photoresist coating, an adhesive polymer namely Hexamethyldisilazane (HMDS) is used to remove OH^- bonds from the substrate surface and form a hydrophobic surface for better adhesion of photoresist [44]. After HMDS, AZ5214E is applied to sample by using spin coater. Laurell spinner system used for photoresist coating is shown in the Figure 2.6.

2.1.4.4 Pre-exposure Bake

Before UV exposure step, pre-exposure bake is applied to remove the remaining solvent, improve resist adhesion, avoid mask contamination due to resist sticking [45]. Samples were put into oven which is at 110^oC for pre-exposure bake. The bake duration was 60 seconds.

Figure 2.7: EVG 620 Mask Aligner

2.1.4.5 UV Exposure

After pre-exposure bake, the photoresist coated samples were exposed using the constant dose mode (50 mJ/cm^2) of mask aligner. EVG 620 mask aligner system used in photolithography step is shown in Figure 2.7.

2.1.4.6 Developing Step

For development of UV exposed photoresist 1:4 mixture of AZ400K and H$_2$O were used. After UV exposure, exposed part of the photoresist becomes less or more soluble in the developer solvent according to tone of photoresist and desired pattern is obtained.

2.1.4.7 Lift-off Step

Developed samples were put into acetone after contact material deposition. The lift-off duration was 2 hours. Then samples were sonicated 5 minutes with refreshed acetone. This step was repeated 3 times for each sample. Finally sample were washed with DI water and dried with nitrogen gas.

2.2 Microfabrication of Resistors

In this section, microfabrication steps of interdigitated resistors are introduced in the section 2.2.1.

2.2.1 Planar Resistors

Microfabrication of planar resistors starts with the Piranha-HF and solvent cleaning of the Silicon wafer. After cleaning, SiO_2 insulation layer was coated by using PECVD system. Before deposition of active material layer (TZO), piranha and solvent cleaning were repeated. Active material was deposited using ALD Savannah system, deposition temperature was selected as 200^oC. After active material deposition, solvent cleaning was repeated. Patterning was done by applying standard photolithography steps and using lift-off mask. Contact material deposition was done by Thermal Evaporator system and this step was followed by lift-off. The microfabrication steps of planar resistors were given in the Figure 2.8.

2.3 Characterization Methods

In this section X-ray Photoelectron Spectroscopy for elemental characterization of deposited thin films and Grazing Incidence X-ray Diffraction for structural characterization of TZO films are introduced in 2.3.1 and 2.3.2.

2.3.1 X-ray Photoelectron Spectroscopy

X-ray Photoelectron Spectroscopy (XPS) is widely used surface analysis technique to determine elemental composition of material, chemical state of elements in material, empirical formula of material, species that contaminate material surface. It is also possible that to make depth profile analysis and determine thin film

Silicon substrate

After oxide deposition

After photolithography

After TZO deposition

After metallization

After lift-off

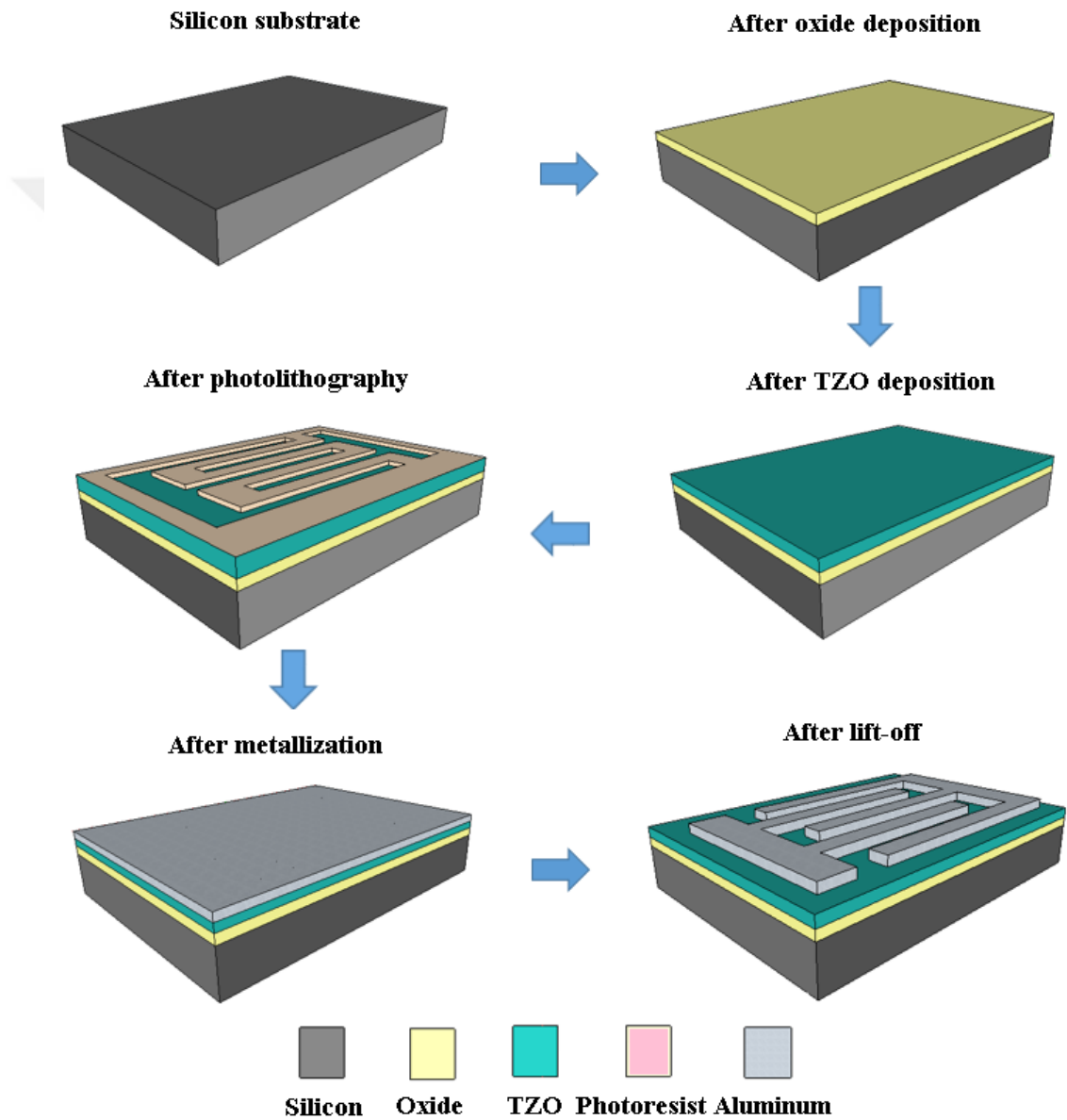| Silicon | Oxide | TZO | Photoresist | Aluminum |

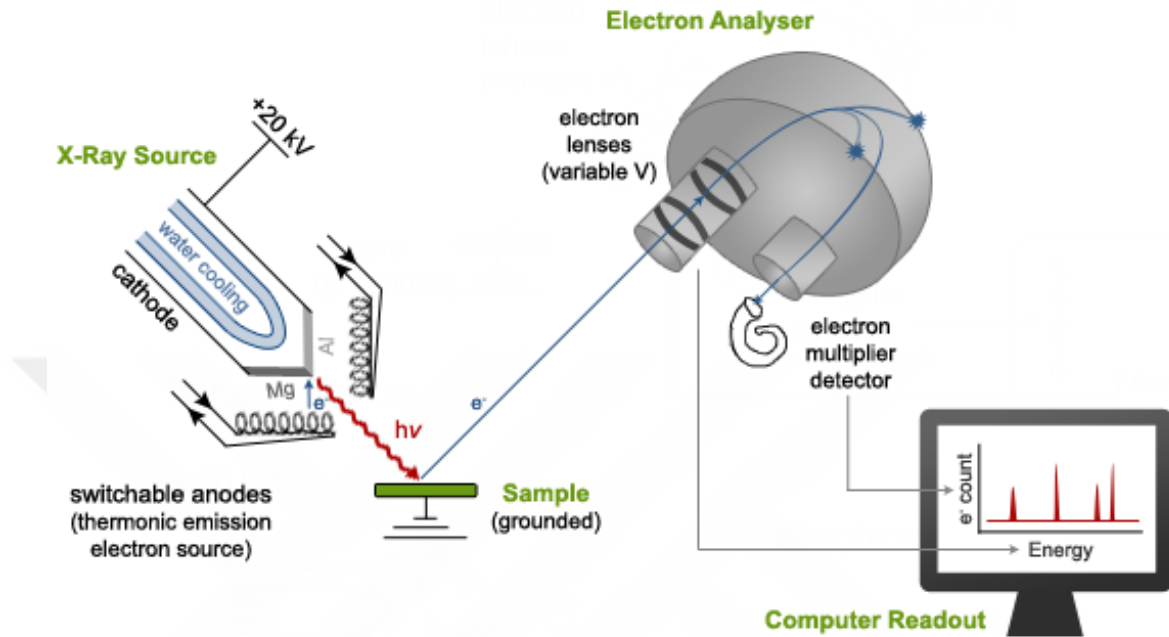Figure 2.8: Microfabrication steps of planar resistors

Figure 2.9: Representative drawing of X-ray Photoelectron Spectroscopy system [46]

elemental composition uniformity by using argon ion beam etching.

The working principle of XPS depends on exciting the sample surface with monochromatic x-ray source and measuring the kinetic energy and intensity of emitted photoelectrons by using electron energy analyser. From kinetic energy of photoelectrons it possible to calculate binding energy of them from the well-known equation of Ernest Rutherford. XPS experiments are performed at high or ultra high vacuum.

$$E_B = hv - E_K + W \qquad (2.1)$$

Where E_B is binding energy of the emitted photoelectron, E_K is kinetic energy of the emitted photoelectron, hv is the energy of x-ray photon, W is the work function is the adjustable instrumental correction factor depends on spectrometer. The working principle of XPS can be better understood from the Figure 2.9 [46].
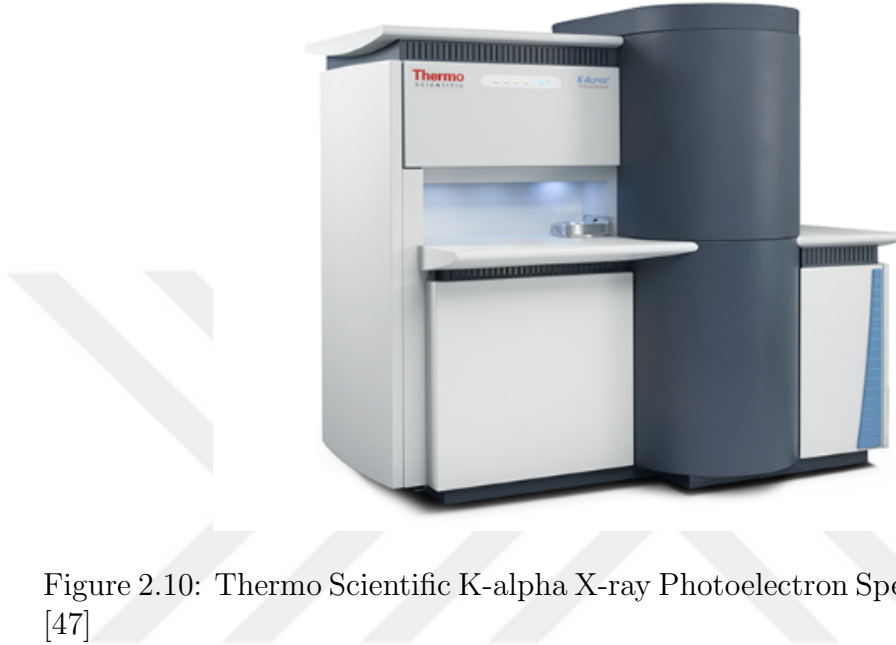
24

Figure 2.10: Thermo Scientific K-alpha X-ray Photoelectron Spectroscopy System [47]

In elemental analysis of deposited thin films, Thermo Scientific X-ray Photoelectron Spectroscopy system with monochromatic Aluminum K_α x-ray source was used. For depth profile analysis, 1kV acceleration voltage was applied to a beam of Argon ions with 400 micrometer spot size. The XPS system is shown in the Figure 2.10 [47].

2.3.2 Grazing Incidence X-ray Diffraction

X-ray diffraction is used for crystal structure determination, quantative phase analysis, crystallite size and microstrain calculation, phase diagram determination, residual stress analysis. The comparable wavelength of the x-ray radiation and interplanar spacing in crystal structure allows the diffraction. Bragg condition is known as the constructive interference condition as shown in Figure 2.11 [48].
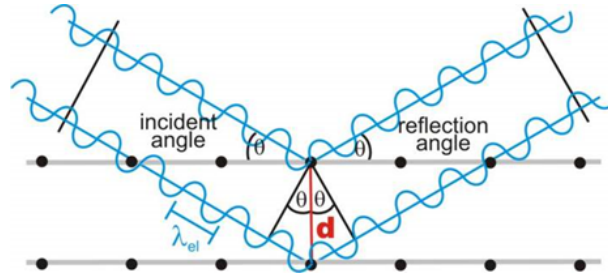
$$n\lambda = 2dsin\theta \tag{2.2}$$

Figure 2.11: Bragg condition for diffraction [48]

The order of reflection is n, the x-ray radiation wavelength is λ, the interplanar spacing is d and the angle between the x-ray beam and specimen surface is θ in Bragg's law.

The x-ray radiation penetration depth through the sample is between 10-100 μ. The x-ray penetration depth is much thicker than deposited thin films, which results in collection of substrate dominant data. Hence bulk X-ray diffraction techniques are not suitable for thin film x-ray diffraction analysis. The path travelled by x-ray in thin film structure is longer in grazing incidence x-ray diffraction technique, because the incidence angle of the x-ray beam is so small [49].

For structural analysis of deposited thin films, PANanalytical X'Pert PRO Materials Research Diffractometer was operated at 45 kV and 40 mA with Copper K_α x-ray source. First fast scan was performed with 0.1 step size and 0.5 second counting time. Then for crystalline samples the measurement was repeated with 0.05 step size and 5 second counting time. Materials Research Diffractometer system used for structural analysis is shown in the Figure 2.12 [50].

Figure 2.12: PANanalytical's X'Pert PRO Materials Research Diffractometer [50]

Chapter 3

Active Material Characterization

In this chapter stability of oxides from thermodynamic point of view, ALD recipe optimization for doping of ZnO, elemental and structural characterization of deposited films are introduced in the sections 2.1, 2.2, 2.3 and 2.4 sequentially.

3.1   Ellingham Diagram of Oxides

Ellingham diagram is a very practical tool using in extractive metallurgy to determine thermodynamic conditions of oxidation, sulfidation and nitrification reactions. Ellingham diagram of oxides are plotted according to the thermodynamic driving force of oxide formation of different metals. Therefore it is possible to determine relative stability of metal oxides from Ellingham diagram [51]. The Ellingham diagram of oxides was shown in the Figure 3.1 [52]. The more negative standard energy means thermodynamically more favorable oxide formation. Therefore it is obvious to say that for all temperatures titanium oxide is thermodynamically more stable than ZnO. Titanium was selected as dopant for ZnO because thermodynamically more stable nature of it may cause reduction in oxygen related defects in ZnO and improve the TCR property of ZnO.
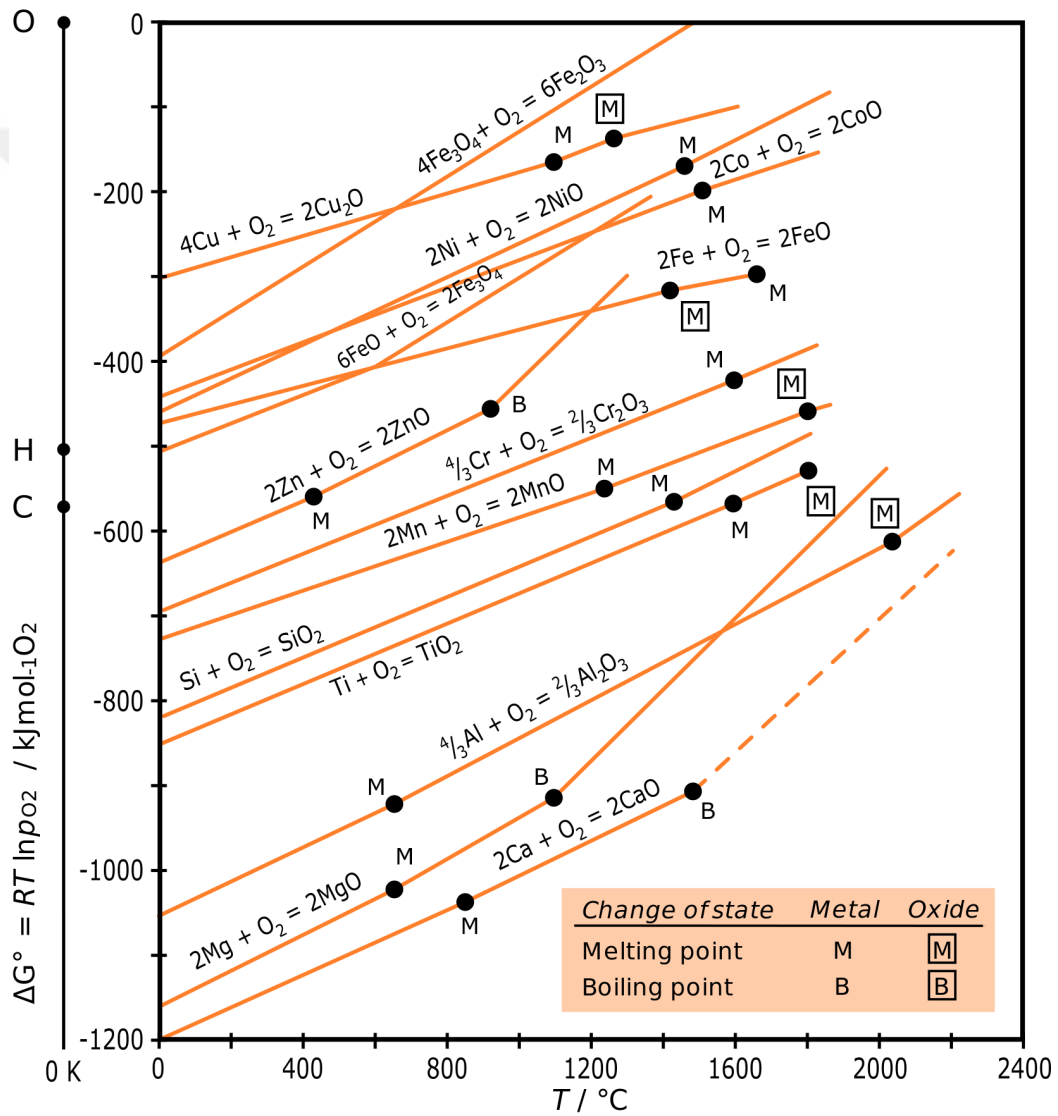
Figure 3.1: Ellingham diagram of metal oxides [52]

29

3.2 ALD Recipe Optimization

For ZnO deposition, organometallic precursor diethylzinc and mili-Q water were used. Deposition temperature was selected as 200^oC for both electrical and chemical stability. Before deposition temperature was stabilized at 0.25 mT using N_2 carrier gas with a flow rate 20 sccm. Pulse time of organometallic precursor and mili-Q water was 0.015 second followed by 10 second purge period. For Titanium doping, the precursor tetrakis(dimethylamido)titanium which was preheated to 75^oC and mili-Q water were used. Both temperature of titanium precursor and chamber were stabilized at 0.25 mT using N_2 carrier gas with a flow rate 20 sccm. Pulse times for organometallic precursor and water were 0.1 and 0.015 second followed by 10 second purge period. These recipes were deposited using different ratios for example (3:1), (5:1), (10:1) followed by elemental characterization to find amount of Ti in ZnO. Finally TZO thin films with 2.5%, 5.9% and 12.2% titanium concentrations were obtained.

3.3 Elemental Characterization

X-ray Photoelectron Spectroscopy (XPS) was used to determine elemental composition, chemical state of deposited Titanium doped Zinc oxide (TZO) thin films and finally intrinsic defect related study of TZO films was carried according to Titanium concentration.

Survey scans of all deposited films contains zinc (Zn), oxygen (O), titanium (Ti) and carbon (C) at surface level. Presence of carbon at surface level is due to surface contamination. Depth profile analysis was carried out to indicate both surface carbon contamination and the uniformity of deposited thin films. Sputtering of thin films was conducted using Argon ion beam with acceleration voltage and spot size of 1 kV and 400um. Carbon was not detected in the bulk film as expected. Elemental composition of deposited bulk films was given in the Table 3.1 above. Uniform thin film composition was observed for all deposited thin

Sample	Zn (at.%)	O (at.%)	Ti (at.%)	Ar (at.%)	C (at.%)
T1	49.4	46.3	2.5	1.8	0
T3	33.1	53.2	12.2	1.5	0
T5	45.3	47.3	5.9	1.5	0

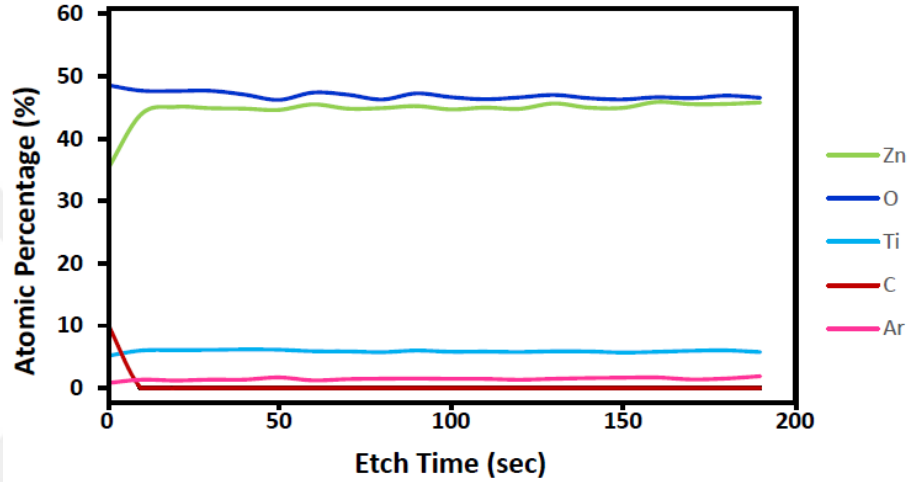Table 3.1: Atomic concentrations of deposited TZO films

Figure 3.2: Depth profile analysis of sample T5 via Argon ion sputtering

films. Depth profile analysis of sample T5 was illustrated in the Figure 3.2.

Deposited TZO films were subjected to XPS analysis of Zn 2p, Ti 2p and O 1s to determine chemical state of substances in deposited films. Adventitious C fit was applied for all samples by setting C 1s peak value at 284.8 eV for internal charge correction.

Zn 2p core level spectrum was obtained from the sample T3 and data was fitted with a single peak as shown in the Figure 3.3. Subpeak with a binding energy of 1021.9 eV is consistent with the literature and confirms the presence of Zn-O bond in film [53, 54].

Ti 2p core level XPS spectrum was deconvoluted into three peaks and the first two corresponds to $2p_{3/2}$ and $2p_{1/2}$ as illustrated in the Figure 3.4a. The centers of the peaks are 458.7 eV and 464.4 eV which are in good agreement with various studies [55, 56]. Also spin orbit splitting value for Ti (IV), which is 5.7 eV was observed [57]. The symmetric shape and the intensity ratio of the
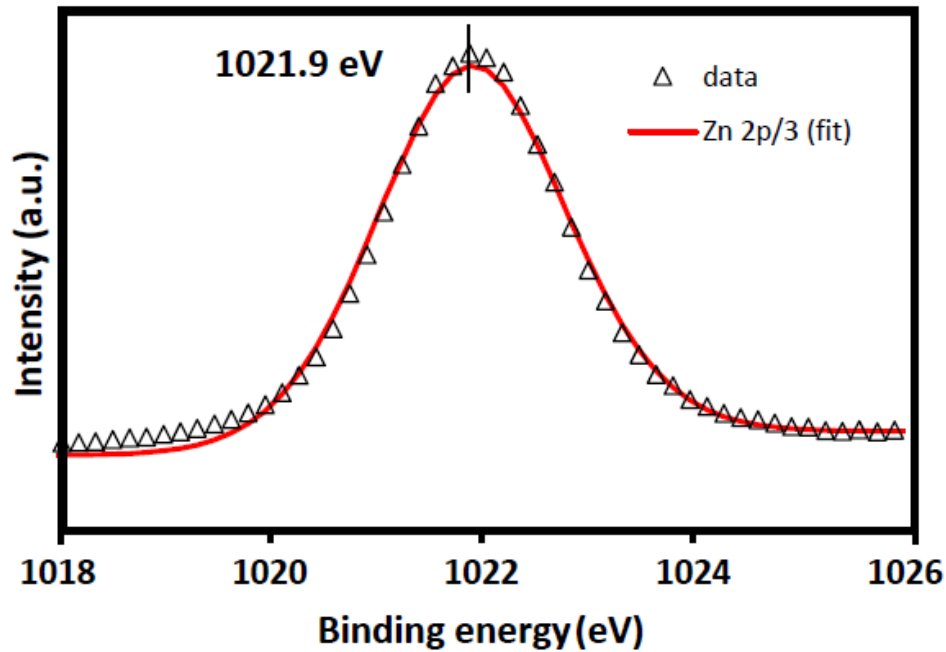
Figure 3.3: Core level XPS spectra of Zn 2p

$2p_{3/2}$ and $2p_{1/2}$ peaks which is 2:1 are in line with the literature. The third peak has so low intensity and high FWHM value that it was shown separately in the Figure 3.4b. The third peak is slightly broader than well-ordered Ti (IV) peaks and corresponds to Ti(III) with spectral location at 456.4 eV. Ti (III) refers to loosely ordered structure.

It is hard to distinguish between O (II) state of titania and zinc oxide because spectral locations of peaks are very close to each other which are 530.4 eV and 530.5 eV. However zinc oxide and titania contain oxygen deficient regions which cause chemisorption of different ions. For titania, it is found that various species containing -OH,-CO, O_2, H_2O adsorbed at these lattice defect sites. Although precise specification of these species is not possible, it is well-known fact that presence of these species produces a peak at 532.4 eV. On the other hand, adsorbed O^-, O^{--} ions at deficient regions of zinc oxide cause to occur a minor peak having spectral location at 531.6 eV [58]. Chemisorption occurred at titania oxygen deficient regions has higher energy which means adsorbed ions bind lattice atoms more tightly. The difference between the spectral locations of adsorbed ions makes possible clear identification of titania and zinc oxide from
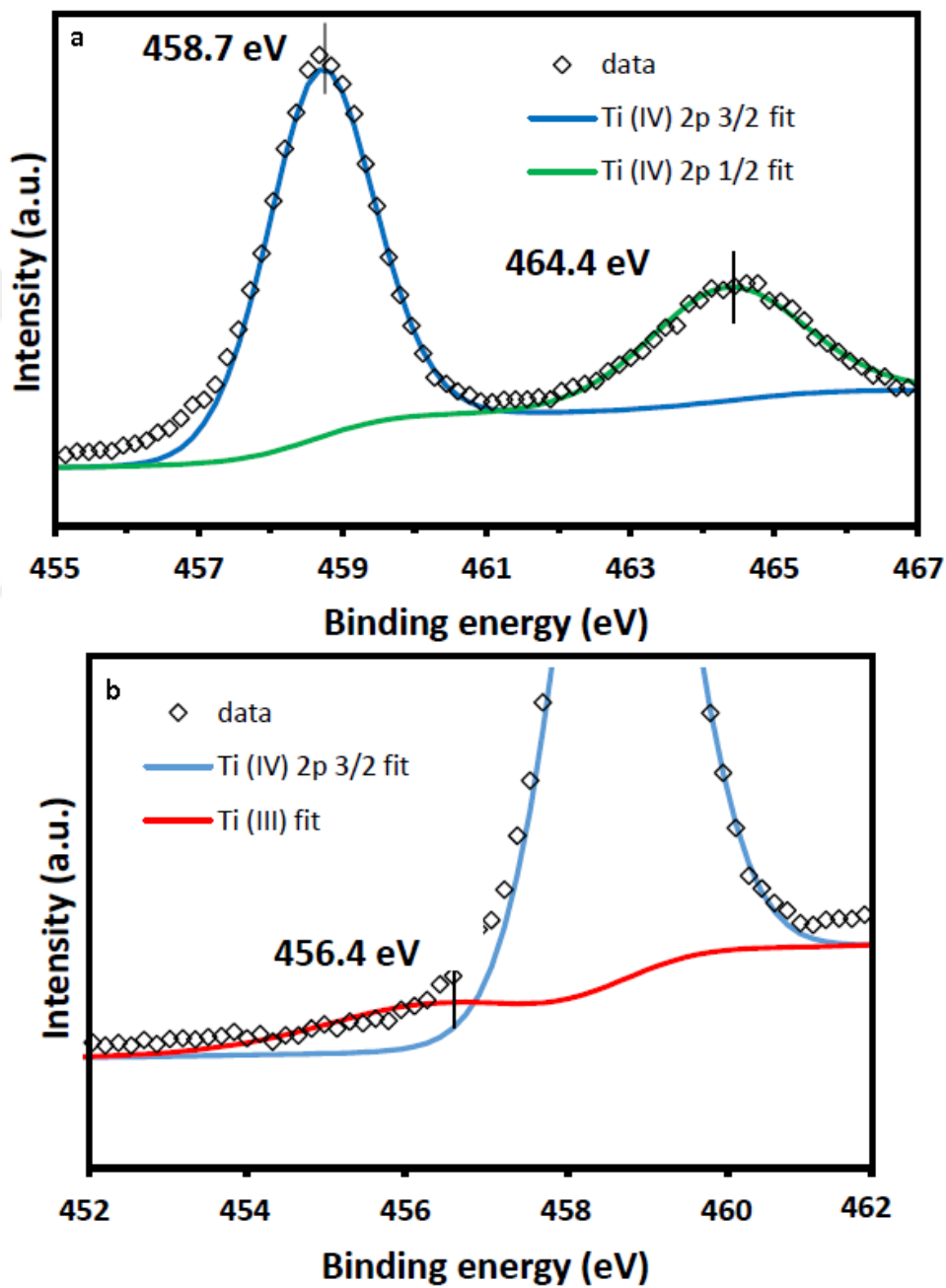
Figure 3.4: Core level spectra of Ti 2p

Ti concentration (at.%)	Ratio of Oxygen defect peak to Oxygen 1s peak
2.5	1:6
5.9	1:18
12.2	1:28

Table 3.2: Ratio of oxygen defect peak for different Ti concentrations

core level XPS spectra of O 1s.

Core level XPS spectra of O 1s is shown as two different graphs in Figure 3.5. Both were deconvoluted into two peaks. In Figure 3.5a the major peak with a binding energy of 530.4 eV refers to O (II) in zinc oxide and the minor peak centered at 531.6 eV corresponds chemisorbed oxygen. Similarly subpeaks with spectral locations at 530.6 eV and 532.4 eV are attributed to oxygen in titania and adsorbed ions in Figure 3.5b. We observe that as titanium concentration was increased in TZO film, the subpeak area ratio of minor and major peak decreased indicating reduction in oxygen related defects. The more favorable oxidation of titanium may cause this reduction. The area ratios of minor and major peaks for different titanium concentrations were given in the Table 3.2.

In summary Zn 2p XPS spectra matches with the binding energy value of Zn-O bond in literature. Ti(IV) peaks located at 458.7 and 464.4 eV confirms the presence of titania in ZnO structure. Additional information about the chemical state of titanium was obtained from O 1s XPS spectra which deconvoluted into two peaks and represents Ti-O bond and chemisorbed ions at lattice defect sites. Therefore Ti is present as oxide other than metallic form in ZnO structure.

3.4 Structural Characterization

Grazing incidence X-ray diffraction (GIXRD) was used to determine crystal structure of deposited TZO thin films with various titanium concentrations. Effect of titanium content on crystallinity of samples was discussed. Diffraction data of atomic layer deposited ZnO thin film was used as reference material for better
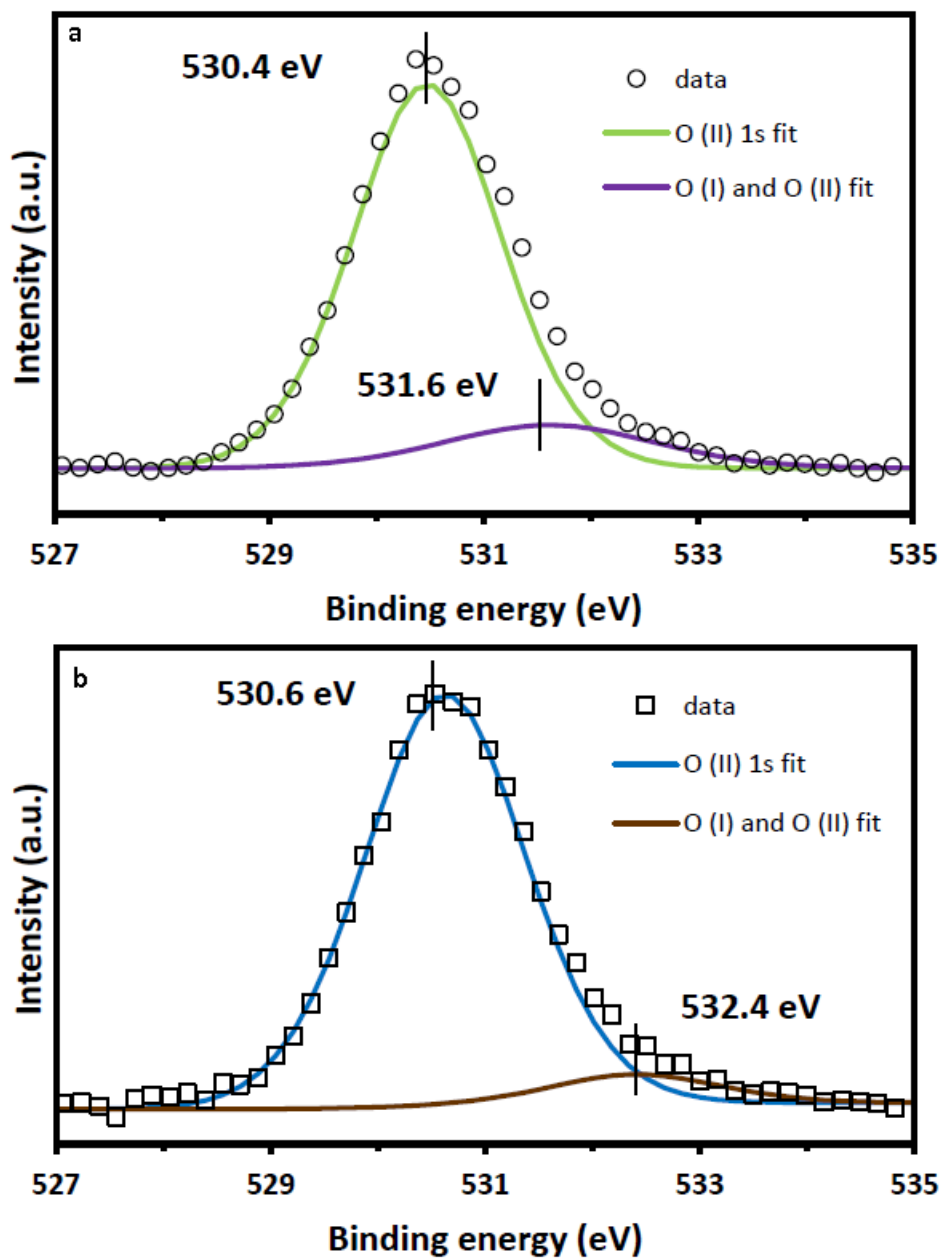
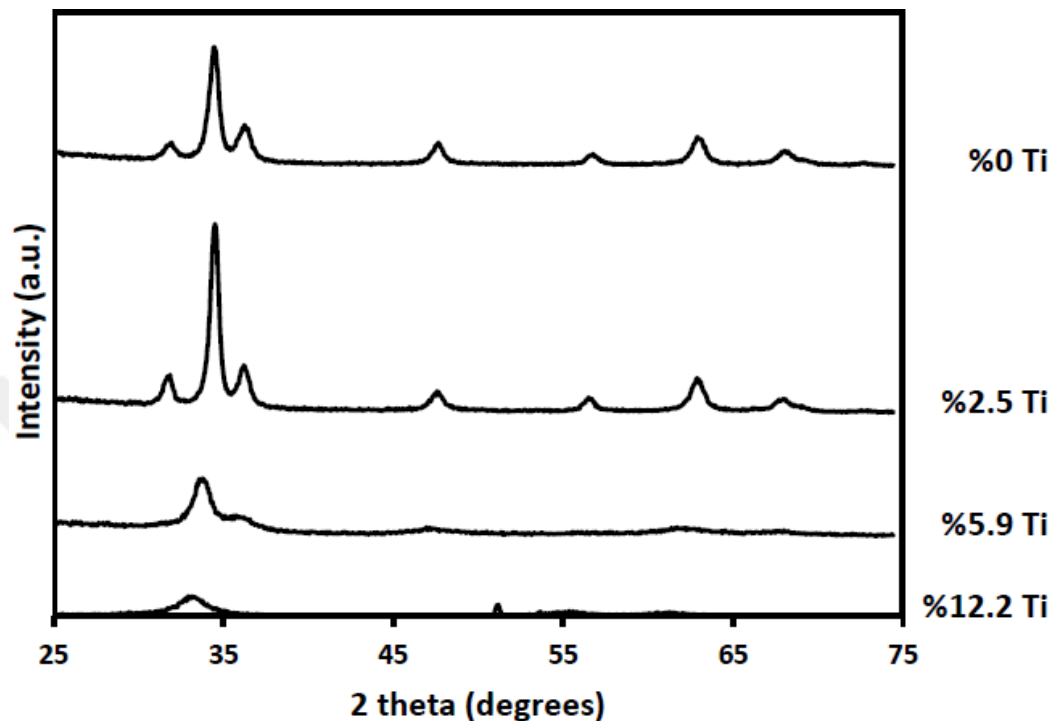Figure 3.5: Core level XPS spectra of O 1s

Figure 3.6: Effect of Ti concentration on TZO film crystallinity

comparison. Interplanar spacing and lattice parameter were calculated for poly-crystalline samples.

Thin film XRD analysis of samples was performed with PANanalytical X'Pert PRO Materials Research Diffractometer with Copper K_α x-ray source. Step size and counting time were adjusted to 0.05 and 5 seconds for all samples. From GIXRD patterns of TZO samples illustrated in the Figure 3.6, hexagonal wurtzite ZnO phase was observed and no phases related to Zn and Ti were detected which was verified by the elemental anaysis. It is known from previous studies that as deposited titania has amorphous nature. Also pure ZnO films deposited at 200°C with ALD and doped ZnO films deposited with another fabrication techniques such as CVD, sputtering have preferred orientation in (002) direction (c axis). It is obvious that, presence of titania in ZnO film cause to appear broad peaks with low intensity indicating distorted crystal structure. Even TZO film with 12.2% Ti concentration is already amorphous.

GIXRD patterns of samples T1 and T5 were carefully inspected and peaks
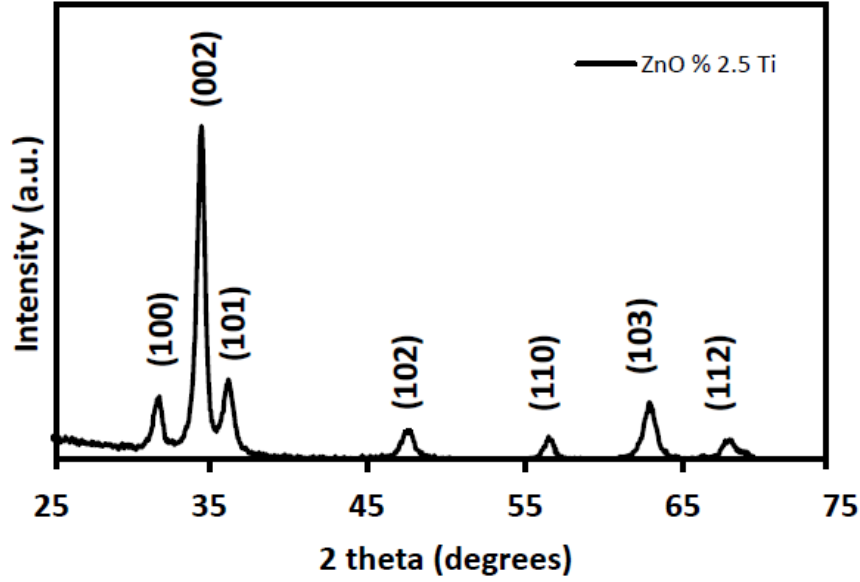
36

Figure 3.7: GIXRD pattern of sample T1

Peak (hkl)	Peak Position (2θ)	d-spacing (Å)	FWHM (2θ)
(100)	31.84	2.81	0.34
(002)	34.52	2.60	0.54
(101)	39.25	2.48	0.39
(102)	47.63	1.91	0.79
(110)	56.47	1.63	0.49
(103)	62.96	1.48	0.69
(112)	68.05	1.38	0.72

Table 3.3: GIXRD analysis of sample T1

were identified by using Expert software as shown in the Figures 3.7 and 3.8. Peak positions matches well with the ZnO wurtzite structure having JCPDS-79-2205 card number. Peak positions, interplanar spacing values, and FWHM values were shown in the Tables 3.3 and 3.4.

Lattice parameters a and c were calculated according to below formula in which d is interplanar spacing and (hkl) are miller indices (hkl). For sample T1, (002) and (100) planes were substituted, for sample T5, (002) and (101) planes were substituted into formula. Calculated lattice parameter values and c/a ratios were given in Table 3.5.
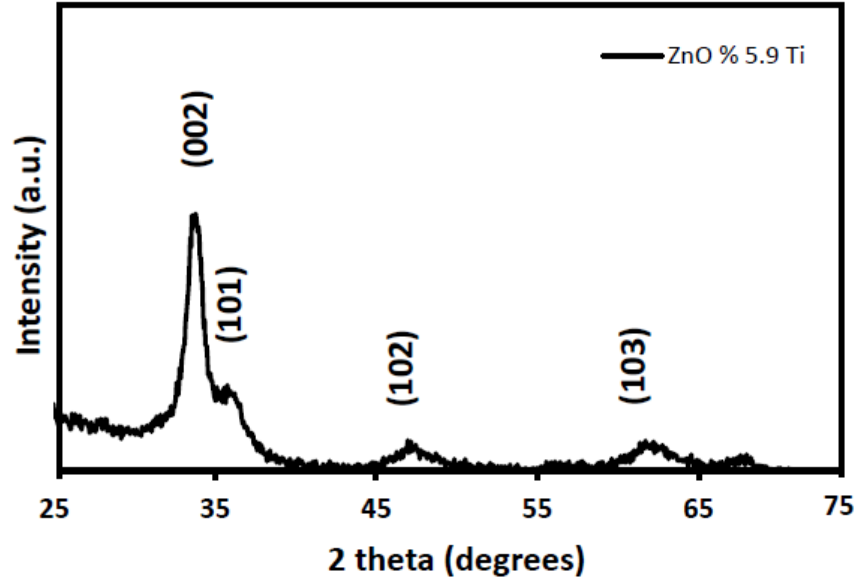
Figure 3.8: GIXRD pattern of sample T5

Peak (hkl)	Peak Position (2θ)	d-spacing (Å)	FWHM (2θ)
(002)	33.60	2.67	0.79
(101)	36.40	2.47	0.98
(102)	47.12	1.93	1.20
(112)	68.10	1.38	1.09

Table 3.4: GIXRD analysis of sample T5

Sample	a (Å)	c (Å)	c/a	unit cell volume (Å³)
Reference	3.24	5.205	1.605	142.274
T1	3.246	5.197	1.601	142.266
T5	3.215	5.334	1.659	143.241

Table 3.5: Lattice parameter values of samples

$$\frac{1}{d^2} = \frac{4}{3}\left(\frac{h^2 + hk + k^2}{a^2}\right)\frac{l^2}{c^2} \tag{3.1}$$

Lattice parameters of samples T1 and T5 is very comparable to that of reference sample. c/a ratios are also consistent with the literature which confirms the hexagonal wurtzite structure of TZO films.

Chapter 4

Electrical Characterization of Fabricated Resistors

In this chapter, current-voltage characterization, calculated resistivity and resistance values, temperature coefficient of resistance (TCR) measurement results of resistors are given.

4.1 Current-Voltage Characterization

I-V curves of samples T1, T2, T3, T5 and T6 were given in this section. The sample T4 is already insulator, so it is not possible to obtain reliable electrical characterization data from this sample.

I-V curve characterization is used to determine the basic parameters of devices. Since a resistor contains metal-semiconductor junction, the most important parameter is contact type. A metal-semiconductor junction should allow the flow of current in both ways with equal amount. In other words, current-voltage curve of a resistor should cross the origin with a constant slope, this contact type is called as ohmic. Possible I-V curves of devices are shown in Figure 4.1 [59].
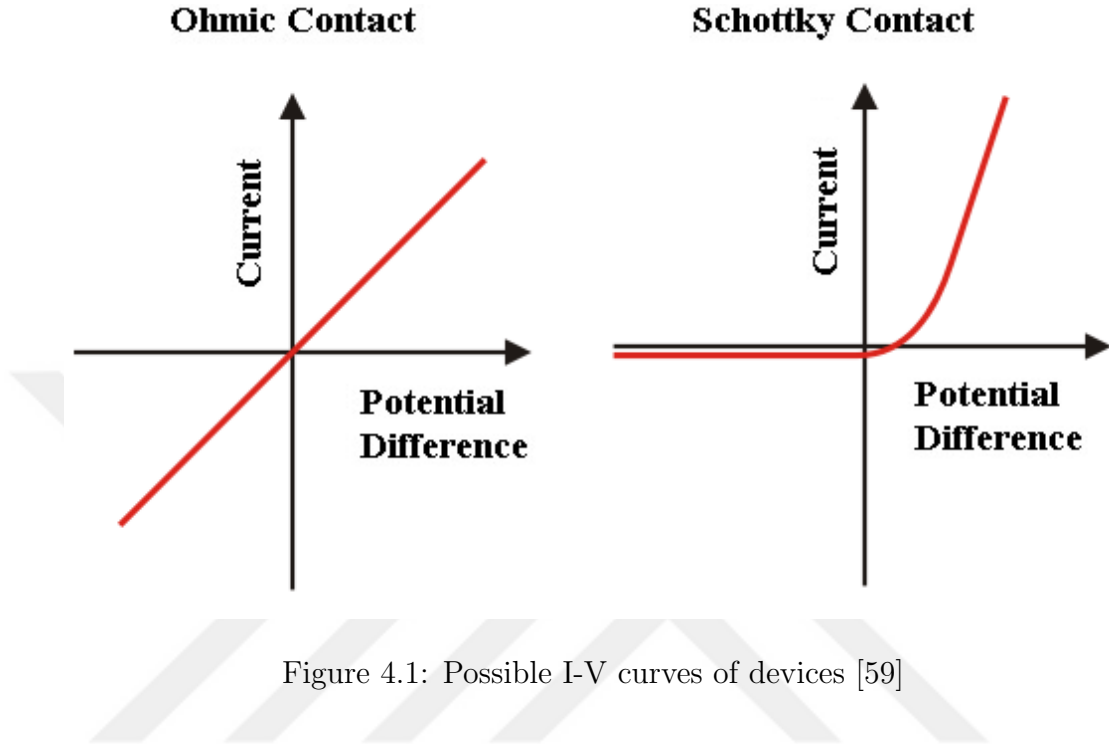
Figure 4.1: Possible I-V curves of devices [59]

Ohmic contact between metal-semiconductor junction also means that the contact resistance is very low and it is independent from applied voltage. Therefore, during temperature coefficient of resistance measurements, all the resistance change due to temperature comes from the semiconductor part, other than metal-semiconductor junction. This makes TCR measurements reliable. Current-voltage curves of T1, T2, T3, T5, T6 are illustrated in the Figures 4.2, 4.3 and 4.4. As seen from figures for all device microfabricated TZO and Aluminum electrode makes ohmic contact.

4.2   Resistivity and Resistance

As mentioned in elemental characterization part, Ti exists in TZO thin films as Titania instead of elemental form. Since resistivity of ALD-grown Titania is approximately 10^6 Ω.cm, with increasing Ti concentration, resistivity of TZO films increases.

The calculated resistivity values of active material candidates with different Ti
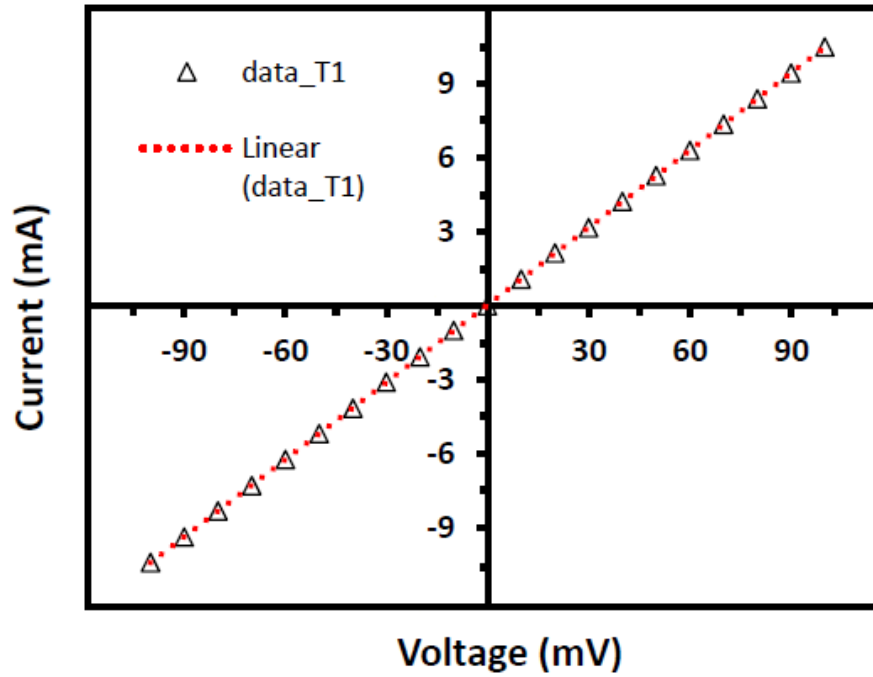
Figure 4.2: Current-voltage curve of T1

Table 4.1: Resistivity values of as deposited samples

Sample	Ti concentration (at.%)	Resistivity (Ω.cm)
T1	2.5	10^{-2}
T5	5.9	10^1
T3	12.2	10^5

doping levels are illustrated in the Tables 4.1. and 4.2. For both as deposited samples and annealed samples the resistivity values of samples raises with increasing Ti concentration as expected.

4.3 Temperature Coefficient of Resistance

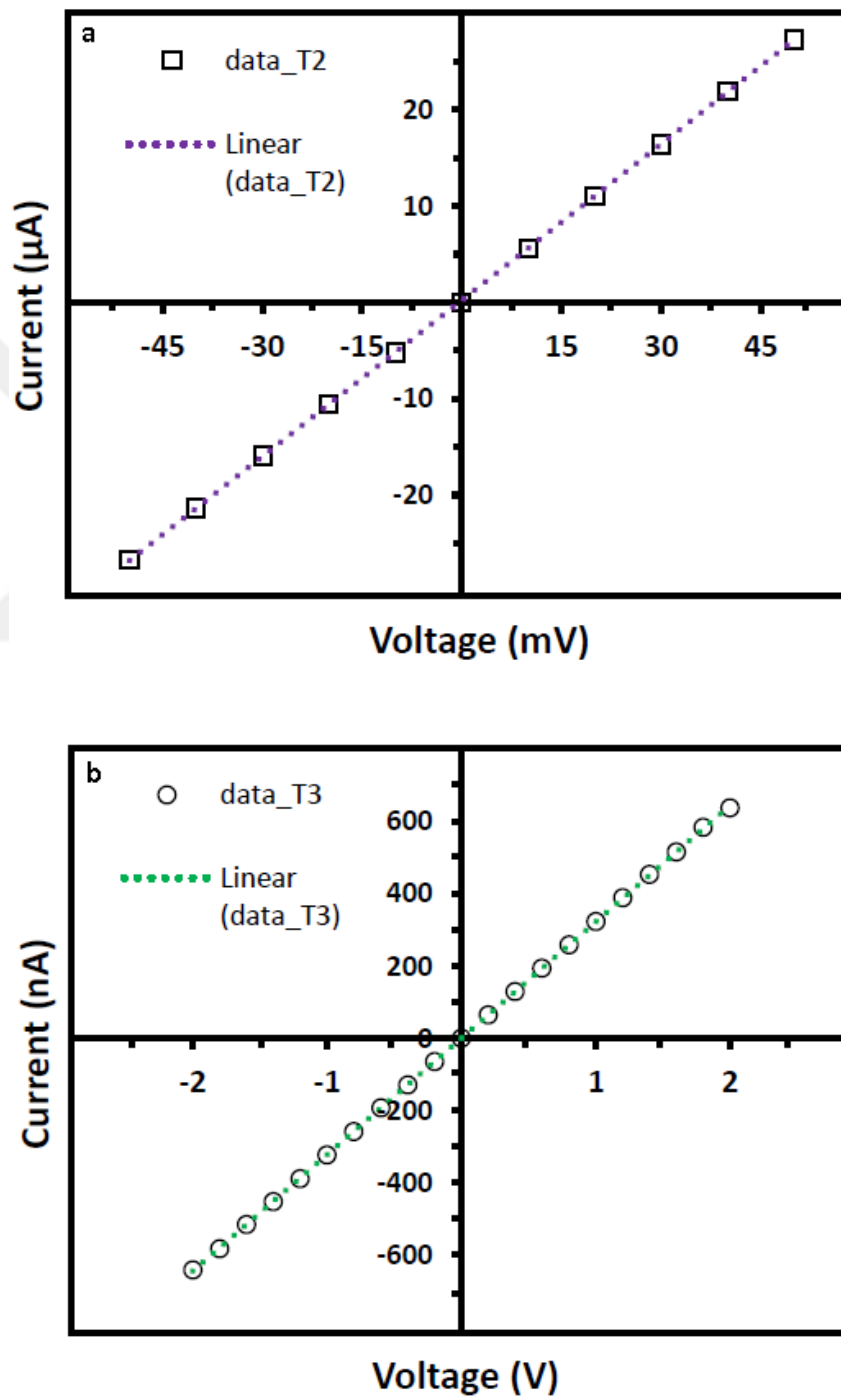Temperature coefficient of resistance measurements of fabricated resistors were done using the following way;
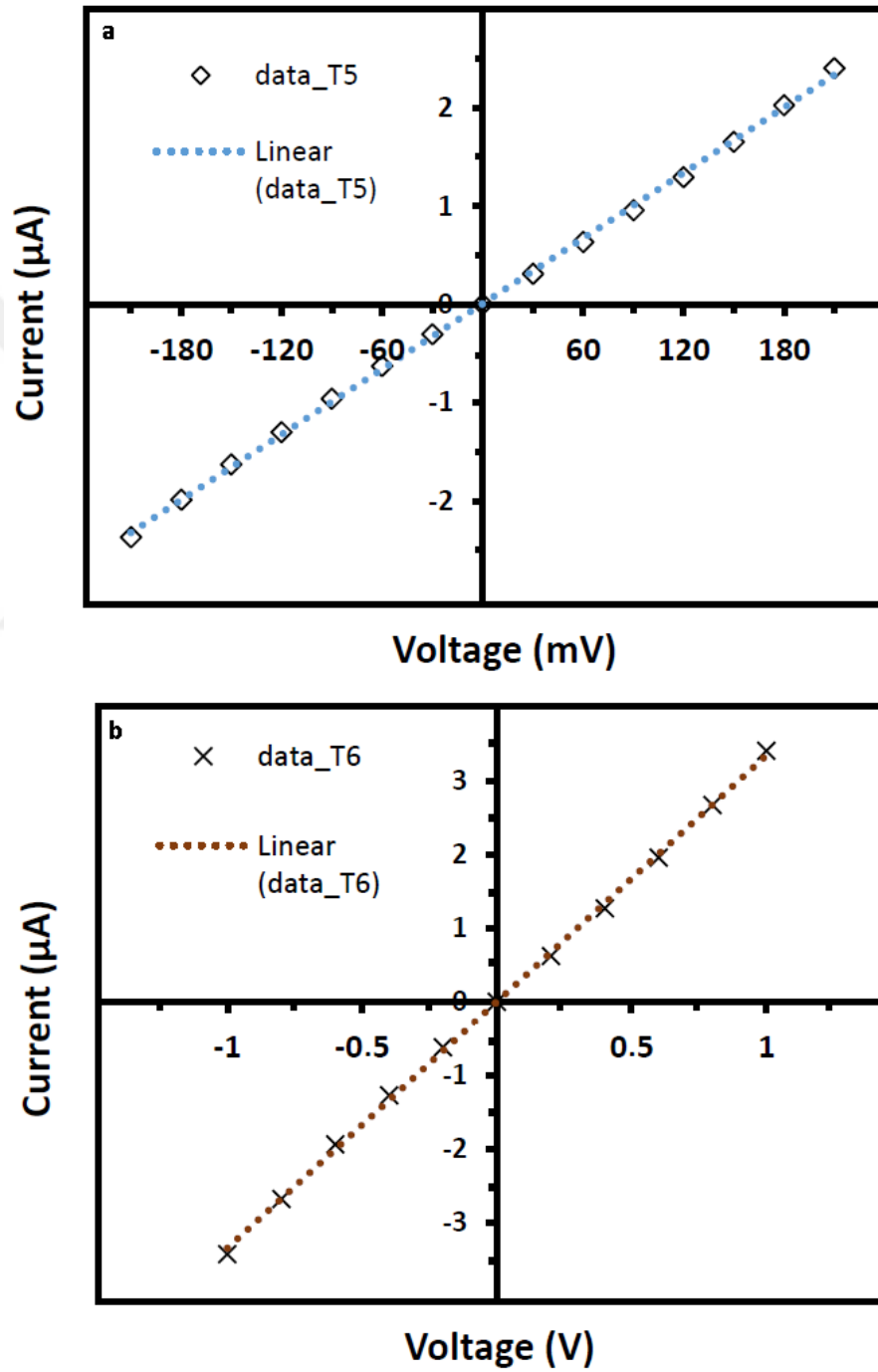
Figure 4.3: Current-voltage curves of T2 and T3

Figure 4.4: Current-voltage curves of T5 and T6

Table 4.2: Resistivity values of annealed samples

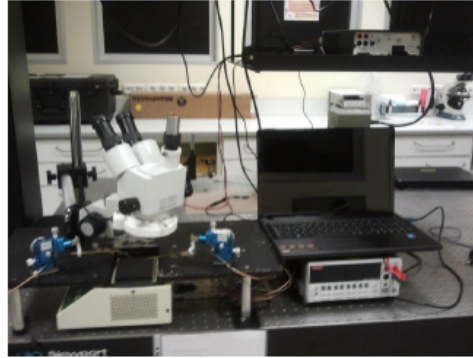| Sample	Ti concentration (at.%)	Resistivity (Ω.cm)
T2	2.5	10^2
T6	5.9	10^5
T4	12.2	very high

Figure 4.5: TCR measurement set-up

1. By the help of microscope, probes are landed on the contact pads of resistor.

2. Constant current is applied between the contact pads and voltage difference is measured using Keithley Sourcemeter.

3. Temperature is increased from 15°C to 24°C using the hot plate and step 1 is repeated for each temperature value.

The TCR measurement set-up is shown in the Figure 4.5. For TCR calculation, first resistance versus temperature graphs are plotted for each sample. TCR values for each temperature is calculated separately. Also an average TCR value is calculated for each sample using the polynomial curve fitting for resistance versus temperature graph. Resistance versus temperature graphs and TCR versus temperature graphs for samples T1, T2, T3, T5, T6 are given in the Figures 4.6, 4.7, 4.8, 4.9, 4.10. Average TCR and resistivity values of samples are listed in Table 4.3.

As seen from the Table 4.3, with raising Ti concentration, temperature coefficient of resistance of TZO thin films increases. Also post-deposition annealed
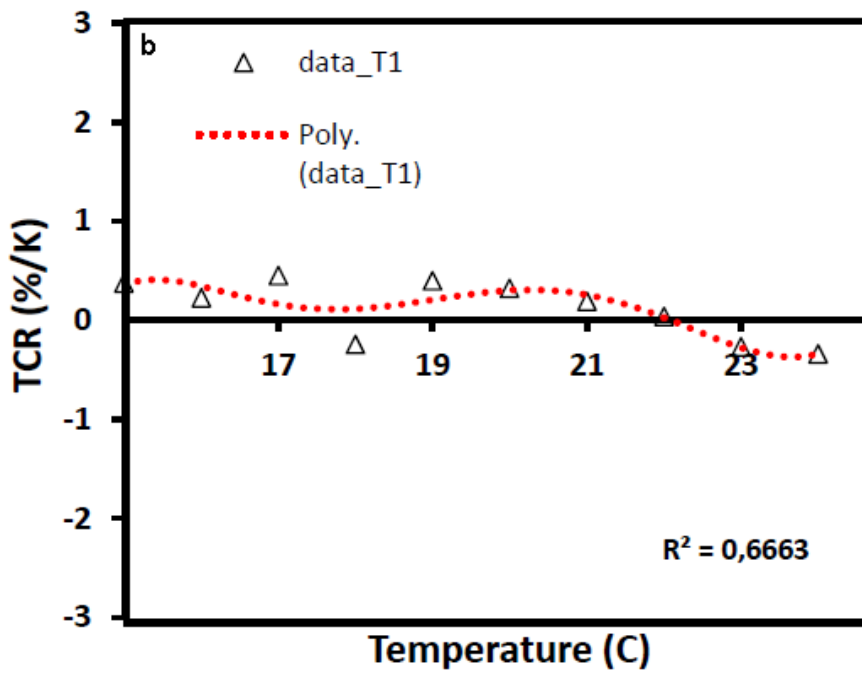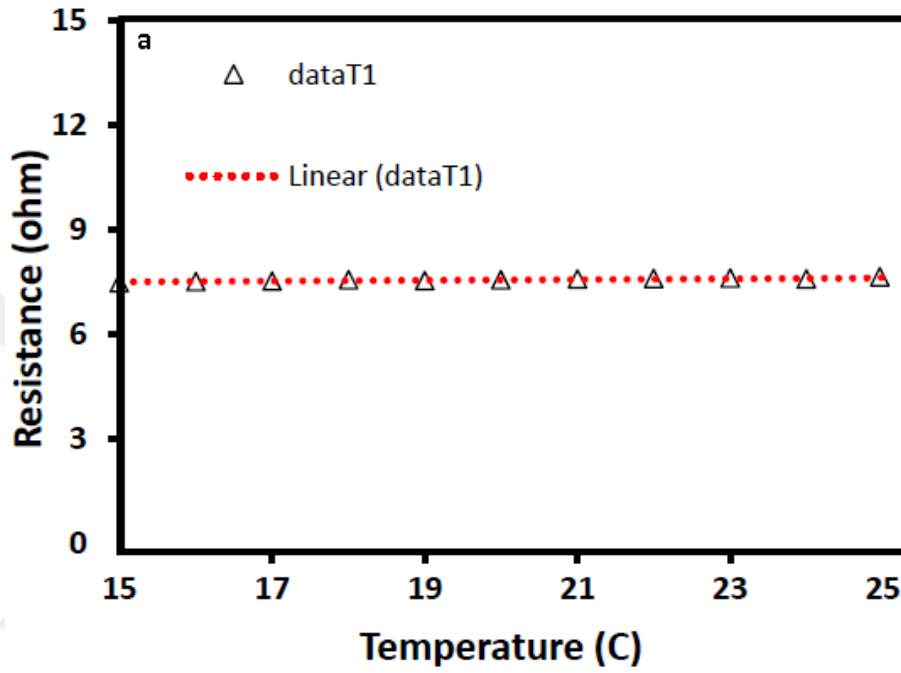
Figure 4.6: Resistance and TCR vs. temperature graphs for sample T1
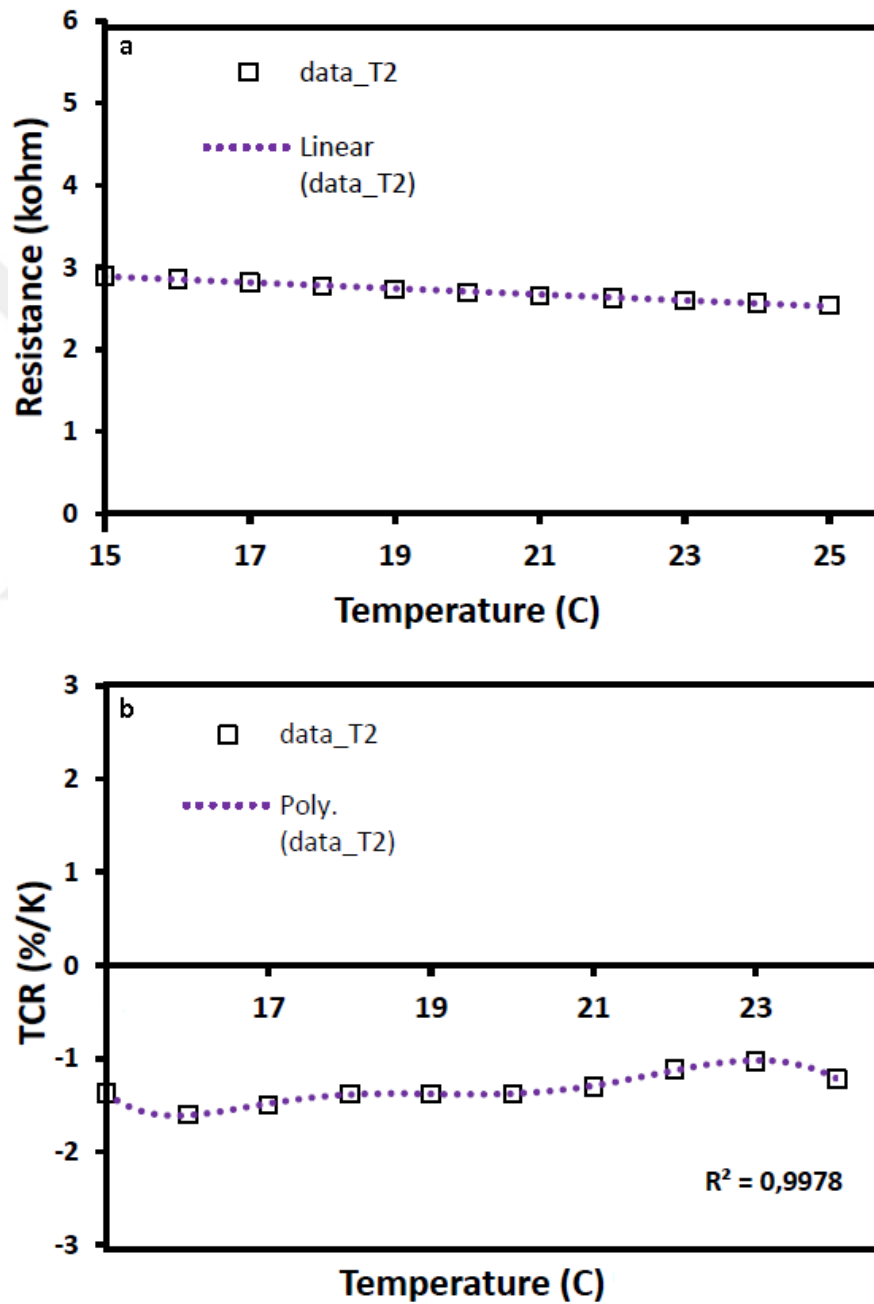
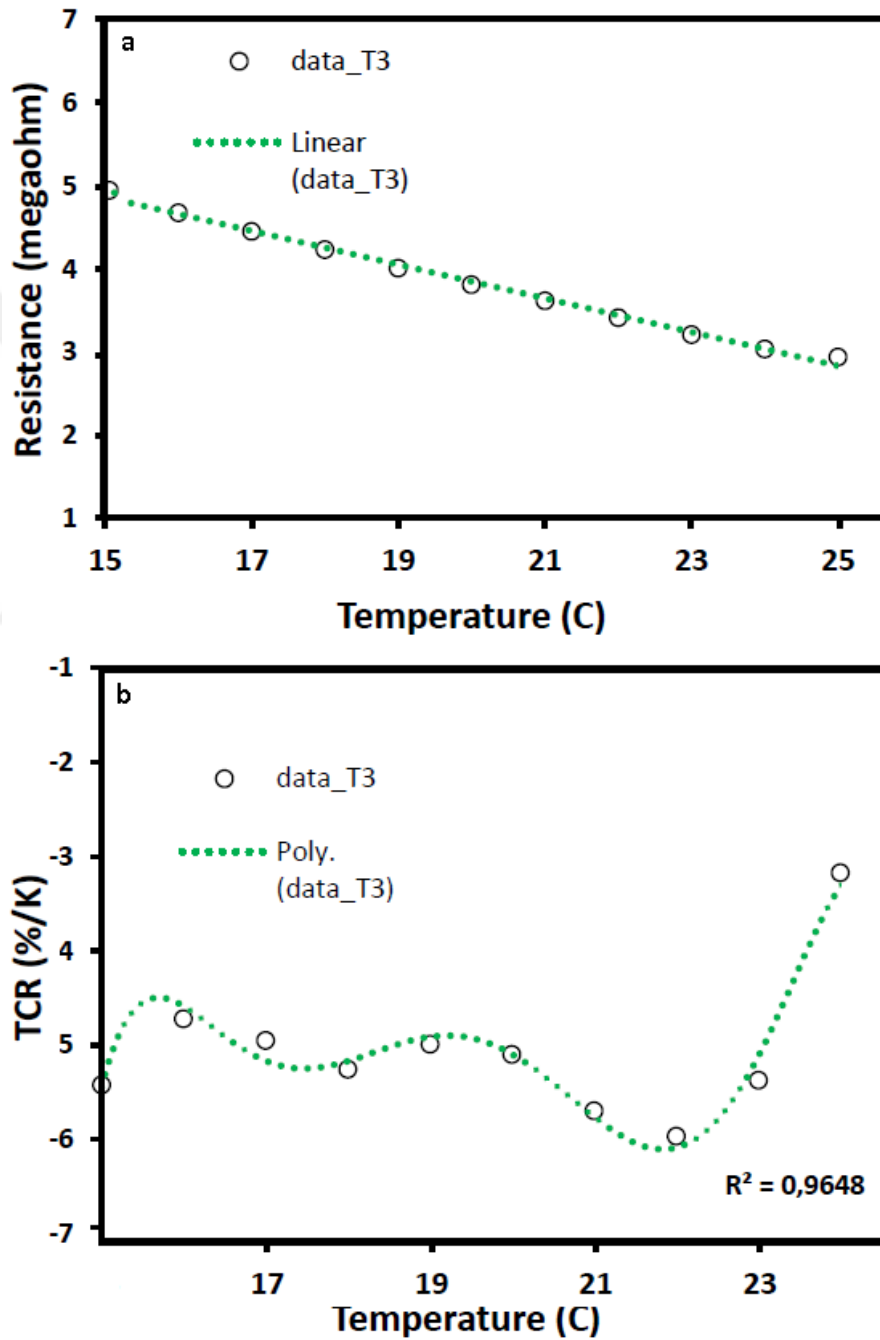Figure 4.7: Resistance and TCR vs. temperature graphs for sample T2

Figure 4.8: Resistance and TCR vs. temperature graphs for sample T3
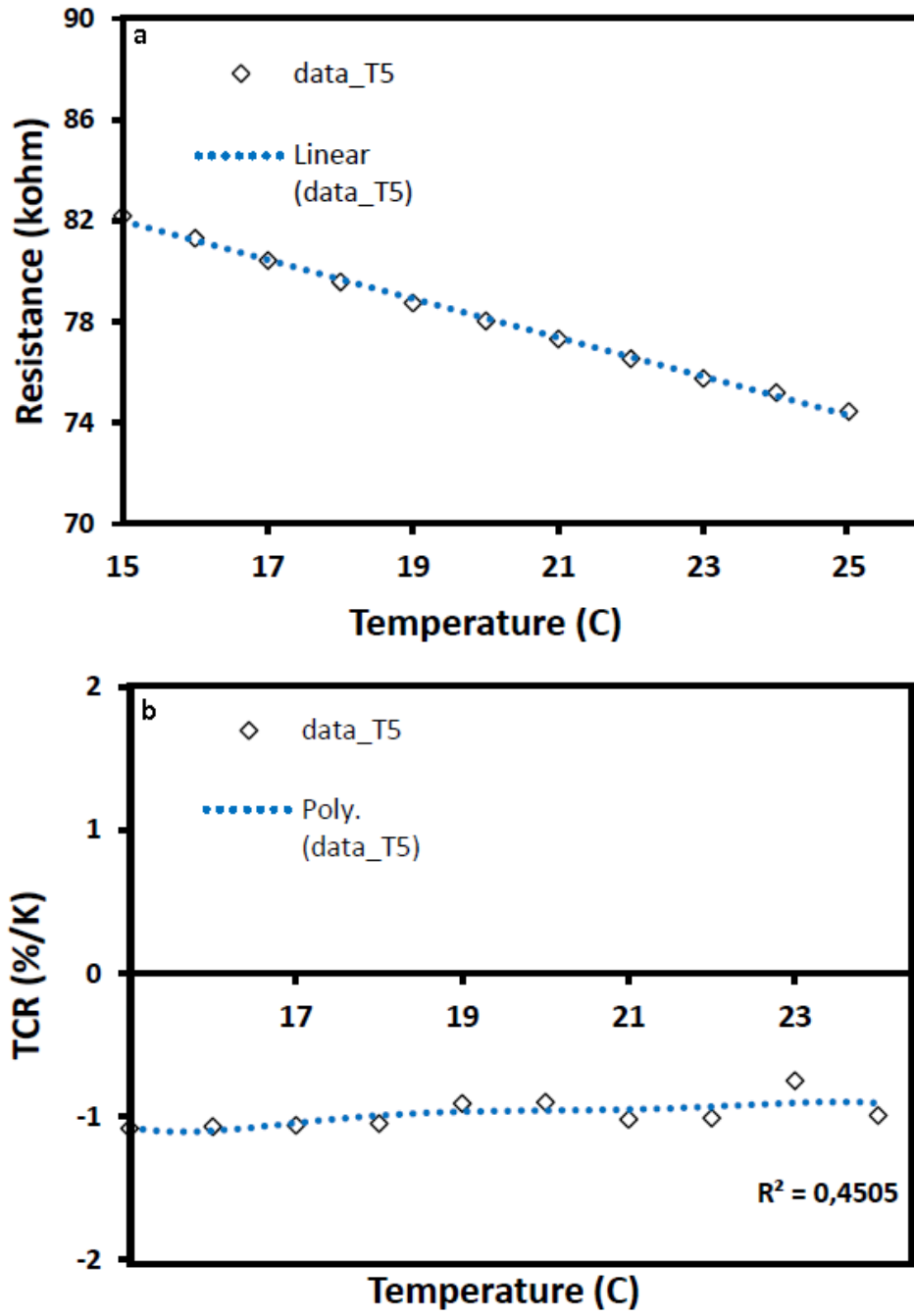
Figure 4.9: Resistance and TCR vs. temperature graphs for sample T5
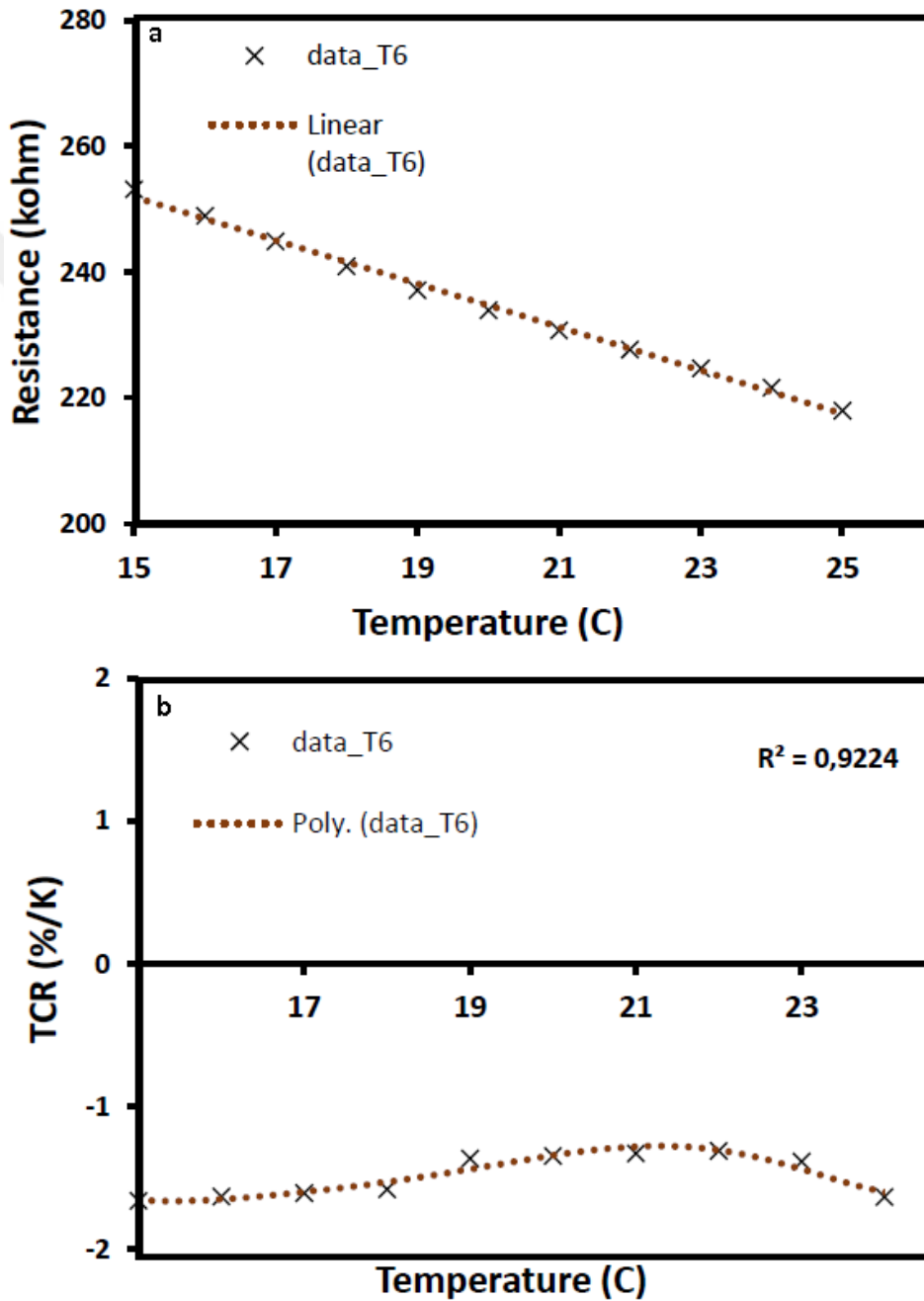
Figure 4.10: Resistance and TCR vs. temperature graphs for sample T6

Sample	Ti concentration (at.%)	TCR (%/K)
T1	2.5	0.12%/K
T5	5.9	0.99%/K
T2	2.5	1.35%/K
T6	5.9	1.47%/K
T3	12.2	5.28%/K

Table 4.3: Average TCR values of samples

samples have higher TCR property than that of as deposited samples. Post-deposition annealing also improves the TCR property.

Since Titanium concentration of the sample T1 is very low, its TCR property is similar to that of pure ZnO deposited at 200°C. Post-deposition annealed samples T2 and T6 have higher TCR value than that of as deposited samples T1 and T5 as expected. Finally sample T3 has the maximum TCR value with -5.96%/K.

Chapter 5

Conclusions and Future Work

ZnO is a strong candidate for optoelectronic applications due to its wide gap with 3.37 eV and the exciton binding energy of ZnO is higher than the commercial materials using in optical applications. ZnO is also an attractive active material candidate for low-cost uncooled thermal detectors due to its high TCR value. Also it is CMOS compatible and has tunable resistivity. However TCR property of pure ZnO is strongly depend on temperature.

In this work, doping ZnO with Titanium was proposed. It was thought that Ti doping may cause reduction in oxygen related defects and improve TCR property of ZnO. Three different TZO films with Ti concentrations 2.5%, 5.9% and 12.2% were achieved. It was demonstrated that presence of Ti in ZnO distorts the crystal structure. It was shown that thin films with 12.2% Ti concentration has higher TCR value than that of commercially available active materials. At the same time, it was observed that TCR of this sample is temperature insensitive in the measurement range between 15°C and 24°C.

To improve the TCR property of pure ZnO, doping materials Hf, Cr, Mn, Al, Mg and Ca are candidates. Doping ZnO with these elements may reduce the oxygen related defects in ZnO structure, since oxides of all these materials are stable than ZnO according to Ellingham diagram of oxides. Manganese oxide

and Chromium oxide involve a variety of oxides because of the different valencies of Mn, Cr and O therefore it is hard to control chemical states of these materials. Aluminum oxide, Calcium oxide and Magnesium oxide are strong electrical insulators, these doping elements may increase the resistivity of ZnO far beyond the semiconductor region . For better resistivity optimization of resultant active material, Hf should be tried first. To homogenize the lattice structure of deposited thin films, post-annealing should be performed. Post-annealing increases the TCR value and smoothens the TCR-temperature curve at the same time. Deposition temperature of the thin film directly affects the chemical state of doping element, defect concentration, resistivity and TCR property, thus different deposition conditions like 150^oC, 200^oC, 250^oC should be tried.

Bibliography

[1] R. from http://www.doitpoms.ac.uk/tlplib/ellinghamdiagrams/applications.php

[2] P. W. Kruse, "Uncooled thermal imaging arrays, systems and applications," SPIE Press, Bellingham, Washington, USA, 2001.

[3] A. Schaufelbuhl, "Thermal imagers in cmos technology," Ph.D. Thesis, ETH Zurich, 2001.

[4] E. Inceturkmen, "A low cost 128x128 infrared detector array in a standard soi cmos technology," M.S. Thesis, Department of Electrical and Electronics Engineering, Middle East Technical University, 2008.

[5] F. Tankut, "Development and characterization of low cost uncooled infrared sensors for commercial applications," M.S. Thesis, Department of Electrical and Electronics Engineering, Middle East Technical University, 2013.

[6] P. W. Kruse and D. D. Skatrud, "Principles of uncooled infrared focal plane arrays," *Semiconductors and Semimetals*, vol. 47, pp. 17–42, Academic Press, San Diego, 1997.

[7] Z. Olgun, "Infrared thermopile structures using any standard cmos integrated circuit process," M.S. Thesis, Department of Electrical and Electronics Engineering, Middle East Technical University, 1998.

[8] R. from https://www.ecnmag.com/article/2015/06/challengesand solutionsthermocouplesignalconditioning

[9] S. Middelhoek and S. A. Audet, "Silicon sensors," Academic Press, London, 1989.

[10] S. R. Hunter and P. G. Datskos, "Mems based pyroelectric thermal energy harvester," 2012. US Patent App. 12/874, 407.

[11] S. B. Lang, "Pyroelectricity: From ancient curiosity to modern engineering tool," *American Institute of Physics*, 2005.

[12] H. C. Wright, "Infrared techniques," Oxford Clarendon Press, 1973.

[13] F. Civitci, "Development of high fill factor uncooled infrared detector pixels," M.S. Thesis, Department of Electrical and Electronics Engineering, Middle East Technical University, 2008.

[14] M. Y. Tanrikulu, "An uncooled infrared microbolometer detector array using surface micromachined mems technology," Ph.D. Thesis, Department of Electrical and Electronics Engineering, Middle East Technical University, 2007.

[15] C. Chen, X. Yi, J. Zhang, and X. Zhao, "Lineer uncooled microbolometer array based on vox thin films," *Infrared Physics and Technology*, vol. 42, pp. 87–90, 2001.

[16] S. A. Dayeh, D. P. Butler, and Z. Celik-Butler, "Micromachined microbolometers on flexible polyimide substrates," *Sensors and Actuators A*, vol. 118, pp. 49–56, 2005.

[17] D. Murphy, M. Ray, A. Kennedy, J. Wyles, R. Wyles, E. Gordon, T. Seller, S. Baur, and D. V. Lue, "High sensitivity 640x512 (20 μm pitch) microbolometer fpas," *Infrared Technology and Applications, SPIE*, vol. 6206, 2006.

[18] A. Heredia, F. J. D. L. Hidalga, A. Torres, and A. Jaramillo, "Low temperature electrical properties of a boron doped amorphous silicon bolometer," *Electrochemical Society*, vol. 61, 2003.

[19] J. S. Shie, Y. M. Chen, M. Ou-Yang, and B. C. S. Chou, "Characterization and modelling of metal-film microbolometer," *Microelectromechanical Systems*, vol. 5, pp. 298–306, 1996.

[20] S. Eminoglu, M. Y. Tanrikulu, and T. Akin, "A low cost 128x128 uncooled infrared detector array in cmos process," *Journal of Microelectromechanical Systems*, vol. 17, 2008.

[21] "Turkish start-ups enter uncooled fpa and roic markets," *Infrared Imaging News*, 2012.

[22] S. Eminoglu, D. S. Sabuncuoglu, M. Y. Tanrikulu, and T. Akin, "Low cost uncooled infrared detectors in cmos process," *Sensors and Actuators A*, vol. 109, 2003.

[23] L. J. Brillson and Y. Lu, "Zno schottky barriers and ohmic contacts," *Journal of Applied Physics*, vol. 109, p. 121301, 2011.

[24] A. Yamada, B. Sang, and M. Konagai, "Atomic layer deposition of ZnO transparent conducting oxides," *Applied Surface Science*, vol. 112, pp. 216–222, 1997.

[25] U. Ozgur, Y. I. Alivov, C. Liu, A. Teke, M. A. Reshcikov, S. Dogan, V. Avrutin, S. J. Cho, and H. Morkoc, "A comprehensive review of zno materials and devices," *Journal of Applied Physics*, vol. 98, p. 041301, 2005.

[26] D. Kim, H. Kang, J. M. Kim, and H. Kim *Applied surface science*, vol. 257, pp. 3776–3779, 2011.

[27] F. Bozkurt-Oruc, L. E. Aygun, I. Donmez, N. Biyikli, A. K. Okyay, and H. Y. Yu, "Low temperature atomic layer deposited zno photo thin film transistors," *Journal of Vacuum Science and Technology A*, vol. 33, no. 1, 2015.

[28] R. B. M. Cross and M. M. D. Souza, "Investigating the stability of zinc oxide thin film transistors," *Applied Physics Letters*, vol. 89, no. 26, 2006.

[29] Y. Liu, S. Mo, R. Yao, and P. T. Lai, "Negative gate-bias instability of zno thin-film transistors studied by currentvoltage and capacitancevoltage analyses," *Journal of Vacuum Science and Technology B*, vol. 32, no. 6, 2014.

[30] X. F. Zhou, H. Z. L. Yong, X. D. Tang, Q. M. Chen, and P. X. Zhang, "Giant temperature coefficient of resistance in zno/si (111) thin films," *Chinese Physics Letters*, vol. 27, no. 1, p. 018101, 2010.

[31] X. Pan, X. Zhao, A. Bermak, and Z. Fan, "Fabrication of a low power cmos-compatible zno nanocomb-based gas sensor," in *2012 IEEE International Symposium on Circuits and Systems*, pp. 3270–3273, May 2012.

[32] B. Liu, C. Liu, J. Xu, and B. Yi, "Temperature coefficients of grain boundary resistance variations in a zno/p-si heterojunction," *Journal of Semiconductors*, vol. 31, no. 12, p. 122001, 2010.

[33] E. Battal, S. Bolat, M. Y. Tanrikulu, A. K. Okyay, and T. Akin, "Atomic layer-deposited zinc oxide as tunable uncooled infrared microbolometer material," *Physica Status Solidi (a)*, vol. 211, no. 11, pp. 2475–2482, 2014.

[34] M. Y. Tanrikulu, H. R. Rasouli, M. Ghaffari, K. Topalli, and A. K. Okyay, "Atomic layer deposition synthesized tiox thin films and their application as microbolometer active materials," *Journal of Vacuum Science and Technology A*, vol. 34, 2016.

[35] S. Bolat, "Electrical properties and device applications of atomic layer deposited zno and gan thin films," M.S. Thesis, Electrical and Electronics Engineering, Bilkent University, 2014.

[36] D. S. Han, D. Y. Moon, Y. J. Kang, J. H. Park, and J. W. Park, "Improvement in the negative bias stability of zinc oxide thin film transistors by hafnium doping," *Current Applied Physics*, vol. 13, pp. S98–S102, 2013.

[37] W. S. Kim, Y. K. Moon, K. T. Kim, S. Y. Shin, B. D. Ahn, J. H. Lee, and J. W. Park, "Improvement in the negative bias temperature stability of zno based thin film transistors by hf and sn doping," *Thin Solid Films*, vol. 519, pp. 6849–6852, 2011.

[38] M. Leskela and M. Ritala, "Atomic layer deposition (ald) from precursors to thin film structures," *Thin Solid Films*, vol. 409, no. 1, pp. 138–146, 2002.

[39] R. from http://www.vaksis.com/?mod=detail techniquesid=20

[40] R. from https://www.imtek.de/professuren/nano/forschung/ aldsurface

[41] R. from http://www.azonano.com/equipmentdetailsaspxEquipID=227

[42] R. from http://www.vaksis.com/?mod=detail techniquesid=17

[43] R. from http://www2.ece.gatech.edu/research/labs/vc/theory/photolith.html

[44] R. from http://www.microchemicals.com/products/adhesion/promotion/hmds.html

[45] R. from http://www.microchemicals.eu/technicalinformation/photoresistbaking.pdf

[46] R. from http://faculty.chem.queensu.ca/people/faculty/horton/research.html

[47] R. from http://sites.cardiff.ac.uk/xpsaccess/services/

[48] R. from http://www.microscopy.ethz.ch/bragg.html

[49] M. Birkholz, P. F. Fewster, and C. Genzel, "Thin film analysis by x-ray scattering," Wiley-VCH, 2006.

[50] R. from http://www.cenimat.fct.unl.pt/services/laboratory-electronic-and-optoelectronic-materials-and-devices/x-ray-diffraction-panalytical-xpert pro

[51] J. Russel and R. Cohn, "Ellingham diagram," Book on Demand, 2012.

[52] R. from https://commons.wikimedia.org/wiki/File:EllinghamRichardsondi agramenglish.svg

[53] J. C. Klein and D. M. Hercules, "Surface characterization of model Urushibara catalysts," *Journal of Catalysis*, vol. 82, no. 2, pp. 424–441, 1983.

[54] "Handbook of x-ray photoelectron spectroscopy," *Physical Electronics Division*, p. 55344, Perkin-Elmer Corporation, 1979.

[55] A. Ayame, H. Suzuki, R. Shinya, and T. Morohashi, "En Japonais," *Bunseki Kagaku*, vol. 40, no. 11, pp. 717–722.

[56] J. L. G. Fierro, L. A. Arrua, J. M. Lopez-Nieto, and G. Kremenic, "Surface properties of Co-precipitated VTiO catalysts and their relation to the selectiveoxidation of isobutene," *Applied Catalysis*, vol. 37, pp. 323–338, 1988.

[57] M. C. Biesinger, B. P. Payne, A. P. Grosvenor, L. W. M. Lau, A. R. Gerson, and R. S. C. Smart *Applied Surface Science*, vol. 257, pp. 2717–2730, 2011.

[58] F. Kayaci, S. Vempati, C. Ozgit-Akgun, I. Donmez, N. Biyikli, and T. Uyar, "Selective isolation of the electron or hole in photocatalysis: Zno–tio 2 and tio 2–zno core–shell structured heterojunction nanofibers via electrospinning and atomic layer deposition," *Nanoscale*, vol. 6, no. 11, pp. 5735–5745, 2014.

[59] R. from http://www.mrcorfe.com/KS4/Phy2/Circuits/IVGraphs.php